Simplified intravoxel incoherent motion (IVIM) diffusion-weighted magnetic resonance imaging for liver lesion discrimination

An analysis of different analysis approaches

Doctoral thesis

to obtain a doctorate

from the Faculty of Medicine

of the University of Bonn

Narine Mesropyan

from Kapan, Armenia

2023

Written with authorization of

the Faculty of Medicine of the University of Bonn

First reviewer: PD Dr. med. Claus C. Pieper

Second reviewer: Prof. Dr. Steffen Manekeller

Day of oral examination: 16.12.2022

From the Department of Diagnostic and Interventional Radiology of University Hospital Bonn

Director: Univ. Prof. Dr. med. Ulrike I. Attenberger

Table of contents

List of abbreviations

IVIM	Intravoxel incoherent motion
MRI	Magnetic resonance imaging
DWI	Diffusion-weighted imaging
ADC	Apparent diffusion coefficient
ROI	Region of interest
I_{ADC}	ADC index maps
ICC	Intraclass correlation coefficient
I_{D}	D′ index maps
I_{Df}	D′ and f′ combined index maps
I_{f}	f′ index maps
D′	Estimated diffusion coefficient
f′	Estimated perfusion fraction
ROC	Receiver operating characteristic
AUC	Area under the curve
CCC	Cholangiocellular carcinoma
CRC	Metastasis from colorectal carcinoma

1. English summary

1.1 Introduction

Magnetic resonance imaging (MRI) of the liver plays a central role in the evaluation of diffuse and focal liver disease. Nowadays, contrast-enhanced MRI has become a standard technique in clinical routine for the detection, discrimination and follow-up of liver lesions. However, contrast agent application is problematic in patients undergoing repetitive examinations and patients with chronic kidney disease. In such circumstances, it would be desirable to gain information without the need for contrast-agent application. Diffusion-weighted MRI (DWI) is a non-contrast technique yielding functional information about the examined tissue (Thoeny und Ross, 2010). DWI is sensitive for the random microscopic motion of water molecules known as Brownian motion. Therefore, differences in water diffusion in different tissue compartments can be measured and compared by calculating the apparent diffusion coefficient (ADC). The degree of diffusion-weighting of the acquired MR-images depends on the so-called b-value with increasing diffusion-weighting the higher the b-values is chosen. For liver imaging, the calculation of the ADC is usually performed with b-values between 0 and 1000 s/mm^2 based on a mono-exponential relationship between signal intensity and the b-value. However, as DWI measures (pseudo)-random motion within the tissue, perfusion (blood flow in small vessels within the tissue) can also contribute to ADC values. To separate these diffusion and perfusion effects the intravoxel incoherent motion (IVIM) theory based on a bi-exponential behavior of signal intensity was proposed by Le Bihan (Le Bihan et al., 1988). Using the IVIM model, a true diffusion coefficient (D), a pseudo-diffusion coefficient (D*) and a perfusion fraction (f) can be calculated. With the growing body of evidence, showing the utility of IVIM-derived parameters not only in discrimination, follow-up and assessment of therapy response of liver lesions, but also in case of breast and prostate cancer as well as gliomas, there is a need for reliable and time-efficient analysis approaches of IVIM-derived parameters (Wang et al., 2016; Cho et al., 2016; Pang et al., 2013). Currently there are several different analysis approaches for IVIM-parameters for reliable liver lesion discrimination. Quantitative IVIM-analysis is usually performed by a region of interest (ROI)-based approach. However, the placement of the ROIs differs between studies (e.g.

ROI-placement into the most diffusion-restricted “hot spots”, ROIs covering the whole lesion, single representative ROI) (Padhani et al., 2009; Mürtz et al., 2018; Mürtz et al., 2019). Furthermore, quantitative assessment of the ROI- data can be performed using mean values by averaging the voxel values or using a histogram analysis (Suo et al., 2016). Apart from time consuming ROI-based analyses, the creation of parametric color-coded maps is another possible approach to allow for quick visual assessment (Ukmar et al., 2017).

The purpose of our studies was to systematically analyze and compare with regard to diagnostic accuracy different ROI-based analysis methods and approaches as well as the use of combined two-color index maps and to evaluate the diagnostic utility of IVIM-derived parameters for liver lesion characterization.

1.2 Materials and methods

1.2.1 Study cohort

This retrospective single center study was approved by the local institutional review board and the need for written informed consent was waived. From 2013 to 2016, consecutive patients with an indication for a liver MRI examination were identified and included in this study if at least one liver lesion ≥ 1 cm other than cysts was detectable. Exclusion criteria were as follows: (1) insufficient imaging quality, including lesions, which are difficult to identify on the DWI and are visible only on one slice; (2) absence of definitive diagnosis (histological and/or imaging features with at least one follow-up examination); (3) local surgery or interventions. Finally, data of 109/73 patients examined at 1.5/3.0 Tesla were analyzed. Patients with following lesions were included: cholangiocellular carcinoma (CCC), hepatocellular carcinoma (HCC), metastasis, focal nodular hyperplasia (FNH), hemangioma. Diagnosis of above-named liver lesions was established based on histological findings and/or typical imaging features according to the current guidelines. A flow-chart of included patients and a table with included lesions are presented in the **Figure 1** and **Table 1** of the 1st manuscript, respectively.

1.2.2 Magnetic resonance imaging and postprocessing

All imaging was performed on clinical whole-body 1.5 Tesla and 3.0 Tesla MRI systems (Ingenia, Philips Healthcare, The Netherlands) using 32-channel abdominal coils with digital interface for signal reception. Besides morphological sequences, DWI was performed with a respiratory-triggered single-shot spin-echo echo-planar imaging sequence with four b values (0, 50, 250, 800 s/mm^2). Detailed scanning parameters are presented in the **Table 2** of the 1st manuscript. In-house written software (MATLAB, MathWorks, Natick, MA) was used for postprocessing, including calculation and construction of color-coded parameter maps. The previously published equations for calculation of IVIM-parameters D and f as well as ADC values from b= 0, 50 and 800 s/mm^2 were used for analysis (Mürtz et al., 2018).

1.2.3 Image analysis

Imaging analysis was performed by two board-certified radiologists (N.M. and C.C.P.) in consensus with a physicist (P.M.). All readers were blinded to the clinical information. One reference lesion per lesion-type per patient was used for analysis. For each lesion, two-dimensional- (2D-) and three-dimensional- (3D-) ROI-based analysis was performed. For 2D-ROI-based analysis one hand-drawn ROI was placed on a single representative slice (reference slice) unaffected by motion and susceptibility artifacts, and pixel misalignments. For 3D-ROI-based analysis hand-drawn ROIs were placed on each slice of the lesion. Slices affected by image artifacts, insufficient imaging quality and/or pixel misalignment between the images with different b-values and/or the two edge slices due to partial volume effects were labeled as „bad“, all other slices were labeled as „good“. The analysis of 3D-ROI data was performed first including all slices (“bad” and “good”), and then including only “good” slices. Analysis of 2D- and 3D-ROIs were performed including centrally deviating areas (e.g., central necrosis, cystic components or scars) and additionally with exclusion of these areas, if they were present (see also **Figure 3** of the 1st manuscript). Furthermore, for each 2D-ROI, histogram analysis including following metrics was performed: median, standard deviation, the 5th, 10th, 25th, 75th, 90th, 95th percentiles, skewness and kurtosis.

1.2.4 Two-color coded index maps: construction and evaluation

Lesions were analyzed in terms of their dignity using two-color coded index maps, which were reconstructed from suitable cut-off values for ADC, D′, and f′, established in the same and previous studies (Mürtz et al., 2018; Mürtz et al., 2019). Assessment of index maps was performed using a 2D-ROI placed on a reference slice. The index maps were displayed as overlay over the DWI b-800 images. A voxel value was set to 100 (displayed as red and indicating malignant structures) if the corresponding parameter voxel value was lower than the determined cut-off value in the index maps. Otherwise, the voxel value was set to 0 (displayed as green and indicating benign structures). A combined index map I_{Df} (combination of I_D and I_f) was created, which shows malignancy only for voxels, which appeared malignant on both index maps ID and If, otherwise benignancy. This means that for I_{Df}, a voxel value was set to 100 if the corresponding voxel values of I_D and If were both 100; otherwise, the voxel value was set to 0. A four-point visual interpretation scale was

used to define the dignity of liver lesions, where “definitely malignant” refers to lesions with definitive dominance of red voxels; “probably malignant” refers to lesions with slightly dominance of red voxels; “probably benign” refers to lesions with slightly dominance of green voxels; “definitely benign” refers to lesions with a definitive dominance of green voxels. Typical examples of liver lesion assessment using two-color coded index maps are given in the **Figures 1** and **2** of the 2nd manuscript.

1.2.5 Statistical analysis

Commercially available software was used for statistical analysis (SPSS, Version 24.0, IBM, pROC package, Version 1.16.2 in R, Version 3.6.1). Student t test and Mann-Whitney U test were used, as appropriate. For liver lesion discrimination into benign and malignant lesions using different ROI- analysis methods, receiver operating characteristic analysis (ROC) was performed. The areas under the curve (AUCs) based on mean ROI values were compared for the different ROI variants. AUCs were compared using the method proposed by DeLong et al (DeLong et al., 1988). Youden’s index was used to determine the optimal cut-off of the ROC curve providing the highest combination of sensitivity and specificity. Histogram analyses were performed in order to investigate whether it may replace manual exclusion of centrally deviating areas in case of mean values and including them in case of histogram metrics. The intraclass correlation coefficients (ICC) were used for the assessment of intra- and inter- reader agreement.

1.3 Results

A total of 54 benign (35/19 at 1.5/3.0 Tesla MRI) and 128 malignant (74/54 at 1.5/3.0 Tesla MRI) liver lesions were analyzed. A total of 47 lesions (36/11 at 1.5/3.0 Tesla MRI) had centrally deviating areas (e.g., central necrosis, cystic components, scars). The diffusion and perfusion parameters of malignant liver lesions were lower than that of benign lesions. ADC provided the highest diagnostic performance for liver lesion discrimination with an AUC of 0.967-0.911, followed by D_1' with an AUC of 0.941-0.857, and f_2' with AUC of 0.731-0.656. All mean values of analyzed IVIM-derived parameters as well as parameters of diagnostic performance statistics for all ROI types at both MRI systems are given in the **Table 3** and **Figure 4** of the 1st manuscript.

1.3.1 Comparison of 2D- vs. 3D-based ROI analysis

We found no significant differences in parameters of diagnostic performance between any types of 2D- and 3D-ROI-based analysis. Even when in 3D-ROI-based analysis only “good” slices were included, the diagnostic performance of IVIM-derived parameters was not superior to that of 2D-ROI-based analysis data. All AUC value comparisons from 2D- and 3D ROI-based analysis are presented in the **Table 4** of the 1st manuscript.

1.3.2 Comparison of ROIs including and excluding centrally deviating areas

Exclusion of centrally deviating areas from ROIs revealed larger AUC values of ADC, D_1', and D_2', for all 2D- and 3D-ROI variants. However, these improvements were significant only at 1.5 Tesla, which might be explained by fewer cases with centrally deviating areas on 3 Tesla MRI. For example, for 2D-ROIs at 1.5 Tesla MRI, AUC values of ADC were improved from 0.925 to 0.958 ($p=0.01$), of D_1' from 0.866 to 0.902 ($p=0.0081$), and of D_2' from 0.822 to 0.864 (0.00089). Examples of liver lesion analysis including and excluding centrally deviating areas are presented in the **Table 5** of the 1st manuscript.

1.3.4 Comparison of mean values vs. histogram metrics

According to the histogram analysis the 5th and 10th percentiles of ADC and D1′ and the 25th percentiles of ADC, D1′ and D2′ lead to significantly higher AUC values than the mean values for ROIs including centrally deviating areas. For instance, following improvements of AUCs were achieved by using the 10th percentile instead of mean value: for ADC from 0.925 to 0.969 (p=0.018), for D_1' from 0.866 to 0.926 (p=0.0042), and for D_2' from 0.822 to 0.856 (p=0.074). For ROIs excluding centrally deviating areas, these improvements were not significant or were achieved to a lesser degree. For instance, following improvements of AUC were achieved by using the 10th percentile instead of mean value: for ADC from 0.958 to 0.975 (p=0.13) and for D_1' from 0.902 to 0.935 (p=0.038). For ADC, D1′ and D2′ no significant differences were found between ROIs excluding centrally deviating areas in case of mean value analysis and including such areas in case of histogram analysis. Detailed parameters of histogram metrics and comparison of diagnostic performances are given in the **Tables 6** and **7** of the 1st manuscript**.**

1.3.5 Quantitative assessment of index maps I_{ADC} and I_{Df}

By using created index maps, similar AUC values of all evaluated IVIM-derived parameters were obtained than by using original IVIM-parameter maps (see also **Table 3** of the 2nd manuscript). For instance, ADC values of malignant lesions were significantly lower than that of benign lesions: 1,124 ± 180 × 10-6 mm^2 /s vs. 1,692 ± 313 × 10-6 mm^2 /s ($p < 0.001$). Therefore, as expected, also the numbers of red voxels on corresponding index maps were significantly higher in malignant than in benign lesions. For instance, following values from index maps were obtained: for I_{ADC} 80% ± 21% vs. 17% ± 25% ($p < 0.001$), for I_{Df} 76% ± 17% vs. 20% ± 18% ($p <0.001$). Although not significant, but in contrast to quantitative assessment of IVIM-derived parameters presented above, I_{Df} revealed the highest diagnostic performance in lesion discrimination with an AUC of 0.975, which was also higher than that of I_{ADC} (AUC: 0.945), P=0.168. Using I_{Df} 93.6% of the lesions were correctly discriminated regarding their malignancy (cut-off value 50.2%), using I_{ADC} only 88.1% of lesions (cut-off value 53.4%). By using the parameter combination of D′ and f′, also 93.6% of the lesions were correctly identified as with I_{Df}.

Detailed parameters of diagnostic performance statistics for all evaluated index maps are given in the **Table 4** of the 2nd manuscript.

1.3.5 Visual assessment of index maps I_{ADC} and I_{Df}

A similar number of lesions was correctly identified by visual assessment as by quantitative assessment using 2D ROIs excluding centrally deviating areas: for I_{Df} 95.4% vs. 93.6%, for I_{ADC} 90.8% vs. 88.1% ($p>0.05$). Diagnostic accuracy of I_{Df} was also higher than that of I_{ADC} by visual assessment: 95.4% vs. 90.8%. Both index maps revealed excellent intra- and inter-observer reliability of the visual judgment with ICC_{intra} of 0.992 for I_{ADC} and 0.989 for I_{Df}; and ICC_{inter} of 0.986 for I_{ADC} and 0.977 for I_{Df}. All ICCs for investigated parameters are given in the **Table 5** of the 2nd manuscript.

1.4 Discussion

The purpose of our studies was to systematically evaluate and compare different ROI-based analysis methods and approaches to find the simplest and most time-efficient and at the same time reliable method for liver lesion discrimination regarding their malignancy using IVIM-derived parameters. The main findings of the presented studies were as follows: (1) IVIM-derived parameters showed equal diagnostic performance by using both 2D- and 3D-ROI based approaches, even if only slices with good imaging quality were included into 3D-ROI based analysis; (2) diagnostic utility of IVIM-derived parameters was higher, if central deviating areas (e.g., central necrosis, cystic components, scars)were excluded; (3) the use of histogram analysis improves the diagnostic utility of IVIM-derived parameters, if centrally deviating areas are not excluded; (4) the created voxel-wise combined color-coded index maps I_{Df} provide the highest diagnostic accuracy for liver lesion discrimination by visual assessment, which was higher to that of I_{ADC} and comparable to that of quantitative analysis of I_{Df}.

IVIM-derived parameters and their high diagnostic performance for the assessment, discrimination as well as follow-up of liver lesions have been investigated innumerous previous studies (Yoon et al., 2014; Zhu et al., 2015; Mürtz et al., 2018; Pieper et al., 2016; Mürtz et al., 2019). However, the application of this promising non-invasive technique in routine clinical practice is significantly limited not only by complexity and time consumption of the quantitative approach but also by the absence of established analysis methods. In general, studies systematically evaluating and comparing different ROI placement and analysis approaches of IVIM-derived parameters for liver lesion discrimination are still missing. The establishment of an appropriate ROI placement and analysis method, which would also provide high diagnostic performance and would be as simple as possible, would enable the broader use of IVIM with its implementation into routine clinical practice. Therefore, in our studies we performed and systematically analyzed different ROI placement and analysis strategies: 2D-ROI based analysis on a single reference slice, 3D-ROI based analysis of the entire liver lesion considering both all and only slices with good imaging quality; first including and then excluding centrally deviating areas (e.g., central necrosis, cystic components, scars). We also generated color-coded index maps and performed quantitative and visual assessment of them.

In the first study, we demonstrated that the diagnostic performance of IVIM-derived parameters is similar using both 2D- and 3D-ROI based approaches, even when by using 3D-ROI based approach only good slices were included into analysis. Similar results have been previously also demonstrated in prostate cancer (Tamada et al., 2018). One of the reasons of this unexpected similar diagnostic performance by using 3D-ROI based approach including and excluding slices with impaired image quality might be explained by the fact that in case of 3D-ROI (including all slices) more slices and, therefore, more voxels were analyzed, which improved the statistics.

The next issue was to investigate whether including or excluding centrally deviating areas has an influence on diagnostic performance of IVIM-derived parameters due to their impact on diffusion and perfusion parameters. Our study results suggest that the exclusion of centrally deviating areas significantly improves the diagnostic utility of IVIM-derived parameters. This might be explained by the fact that these areas, above all necrotic areas contribute to increase of the diffusion coefficient randomly due to the admixture of varied proportions of high values (Gity et al., 2018). For instance, in case of necrotic tumor, the malignancy of tumor may be masked by a higher ADC, obtained from necrotic areas, which leads to false interpretation of lesions` dignity. Therefore, our data suggests that for reliable discrimination of liver lesions the exclusion of centrally deviating areas are necessary.

However, the exclusion of centrally deviating areas may be time-consuming and challenging for young and inexperienced radiologists, and, therefore, is not suitable for routine clinical practice. In this regard, according to previous studies, histogram analysis might be useful (Padhani et al., 2009). We found that using the low percentiles lead to similar diagnostic accuracy for IVIM-derived parameters (ADC and diffusion coefficients) as a mean value analysis of ROIs without centrally deviating areas. Therefore, our study results suggest the use of histogram analysis with low percentiles instead of mean values if centrally deviating areas cannot be excluded manually. This finding also supports the previous data, but in case of breast, testicular cancer and in studies focusing on predicting microvascular invasion of hepatocellular carcinoma (Suo et al., 2016; Fan et al., 2020; Li et al., 2018).

Furthermore, as demonstrated in the previous and present studies, from all single parameters ADC provided the highest discriminatory ability regarding liver lesion malignancy (89.6%). However, even higher discriminatory ability can be achieved by using the combination of D′ and f′ parameters (93.6%). Therefore, in the present studies we used this information for the first time to generate a combined two-color coded index map, which contain information of both parameters D′ and f′ (I_{Df}) for both quantitative and visual assessment of two color-coded index maps. This was possible after we established cutoff values for each parameter using the data of the previous and presented studies (Mürtz et al., 2018; Mürtz et al., 2019). The use of color-coded maps of the perfusion in the stroke diagnostic has been established as a reliable tool for rapid image interpretation (Ukmar et al., 2017). There are already studies, also demonstrating diagnostic value and a potential of index maps, also for the different IVIM-derived parameters (Lee et al., 2015). In our study we also created and evaluated two color-coded index maps. By using the generated color-coded index maps it is only necessary to assess visually whether more or less than half of the voxels in the tumor are red. This allows for a rapid and easy image interpretation and assessment of lesion dignity. As expected, by using I_{Df} similar to quantitative assessment, best diagnostic accuracy was achieved by visual assessment. Excellent intra- and interobserver reliability was achieved. Furthermore, by visual judgment diagnostic accuracy was comparable to ROI-based quantitative analysis, for I_{Df} (95.4% versus 93.6%) and I_{ADC} (90.8% versus 88.1%).

Our studies have several limitations. First, this was a retrospective study in a single-center. Second, although the total number of lesions included was relatively large, only common lesion types were analyzed, which limits the general applicability of our study results. Also, most patients underwent the examination on 1.5 Tesla MRI systems. Therefore, further prospective studies on the both magnetic strength fields on a larger patient’s cohort are necessary to corroborate the results of the presented studies.

1.5 Summary

Diffusion weighted imaging is one of the most promising non-invasive imaging techniques implemented in routine clinical practice and plays an important role in liver lesion characterization and discrimination. Using DWI-derived IVIM parameters, a reliable liver lesion discrimination into benign and malignant lesions is possible. For this purpose, using representative 2D-ROIs is sufficient in routine clinical practice. Centrally deviating areas such as central necrosis, cystic components or scars should be excluded from ROIs either by hand or by computing low percentiles of diffusion coefficients instead of mean values by histogram analysis. Furthermore, created voxel-wise combined index maps I_{Df} and the ROI-based combination of D′ and f′ parameters provide concordant diagnostic accuracy for liver lesion discrimination. The described I_{Df} index map used as two-color overlay to b-800 images can be considered as a new tool for visual assessment and liver lesion discrimination.

1.6 References for the English summary

Cho GY, Moy L, Kim SG, Baete SH, Moccaldi M, Babb JS, Sodickson DK, Sigmund EE. Evaluation of breast cancer using intravoxel incoherent motion (IVIM) histogram analysis: comparison with malignant status, histological subtype, and molecular prognostic factors. European radiology 2016; 26: 2547–2558

DeLong ER, DeLong DM, Clarke-Pearson DL. Comparing the areas under two or more correlated receiver operating characteristic curves: a nonparametric approach. Biometrics 1988; 44: 837–845

Fan C, Min X, Feng Z, Cai W, Li B, Zhang P, You H, Xie J, Wang L. Discrimination between benign and malignant testicular lesions using volumetric apparent diffusion coefficient histogram analysis. European journal of radiology 2020; 126: 108939

Gity M, Moradi B, Arami R, Arabkheradmand A, Kazemi MA. Two Different Methods of Region-of-Interest Placement for Differentiation of Benign and Malignant Breast Lesions by Apparent Diffusion Coefficient Value. Asian Pacific journal of cancer prevention : APJCP 2018; 19: 2765–2770

Le Bihan D, Breton E, Lallemand D, Aubin ML, Vignaud J, Laval-Jeantet M. Separation of diffusion and perfusion in intravoxel incoherent motion MR imaging. Radiology 1988; 168: 497–505

Lee Y, Lee SS, Kim N, Kim E, Kim YJ, Yun S-C, Kühn B, Kim IS, Park SH, Kim SY, Lee M-G. Intravoxel incoherent motion diffusion-weighted MR imaging of the liver: effect of triggering methods on regional variability and measurement repeatability of quantitative parameters. Radiology 2015; 274: 405–415

Li H, Zhang J, Zheng Z, Guo Y, Chen M, Xie C, Zhang Z, Mei Y, Feng Y, Xu Y. Preoperative histogram analysis of intravoxel incoherent motion (IVIM) for predicting microvascular invasion in patients with single hepatocellular carcinoma. European journal of radiology 2018; 105: 65–71

Mürtz P, Pieper CC, Reick M, Sprinkart AM, Schild HH, Willinek WA, Kukuk GM. Is liver lesion characterisation by simplified IVIM DWI also feasible at 3.0 T? European radiology 2019; 29: 5889–5900

Mürtz P, Sprinkart AM, Reick M, Pieper CC, Schievelkamp A-H, König R, Schild HH, Willinek WA, Kukuk GM. Accurate IVIM model-based liver lesion characterisation can be achieved with only three b-value DWI. European radiology 2018; 28: 4418–4428

Padhani AR, Liu G, Koh DM, Chenevert TL, Thoeny HC, Takahara T, Dzik-Jurasz A, Ross BD, van Cauteren M, Collins D, Hammoud DA, Rustin GJS, Taouli B, Choyke PL. Diffusion-weighted magnetic resonance imaging as a cancer biomarker: consensus and recommendations. Neoplasia (New York, N.Y.) 2009; 11: 102–125

Pang Y, Turkbey B, Bernardo M, Kruecker J, Kadoury S, Merino MJ, Wood BJ, Pinto PA, Choyke PL. Intravoxel incoherent motion MR imaging for prostate cancer: an evaluation of perfusion fraction and diffusion coefficient derived from different b-value combinations. Magnetic resonance in medicine 2013; 69: 553–562

Pieper CC, Sprinkart AM, Meyer C, König R, Schild HH, Kukuk GM, Mürtz P. Evaluation of a Simplified Intravoxel Incoherent Motion (IVIM) Analysis of Diffusion-Weighted Imaging for Prediction of Tumor Size Changes and Imaging Response in Breast Cancer Liver Metastases Undergoing Radioembolization: A Retrospective Single Center Analysis. Medicine 2016; 95: e3275

Suo S, Zhang K, Cao M, Suo X, Hua J, Geng X, Chen J, Zhuang Z, Ji X, Lu Q, Wang H, Xu J. Characterization of breast masses as benign or malignant at 3.0T MRI with whole-lesion histogram analysis of the apparent diffusion coefficient. Journal of magnetic resonance imaging : JMRI 2016; 43: 894–902

Tamada T, Huang C, Ream JM, Taffel M, Taneja SS, Rosenkrantz AB. Apparent Diffusion Coefficient Values of Prostate Cancer: Comparison of 2D and 3D ROIs. AJR. American journal of roentgenology 2018; 210: 113–117

Thoeny HC, Ross BD. Predicting and monitoring cancer treatment response with diffusion-weighted MRI. Journal of magnetic resonance imaging : JMRI 2010; 32: 2–16

Ukmar M, Degrassi F, Pozzi Mucelli RA, Neri F, Mucelli FP, Cova MA. Perfusion CT in acute stroke: effectiveness of automatically-generated colour maps. The British journal of radiology 2017; 90: 20150472

Wang M, Li X, Zou J, Chen X, Chen S, Xiang W. Evaluation of Hepatic Tumors Using Intravoxel Incoherent Motion Diffusion-Weighted MRI. Medical science monitor : international medical journal of experimental and clinical research 2016; 22: 702–709

Yoon JH, Lee JM, Yu MH, Kiefer B, Han JK, Choi BI. Evaluation of hepatic focal lesions using diffusion-weighted MR imaging: comparison of apparent diffusion coefficient and intravoxel incoherent motion-derived parameters. Journal of magnetic resonance imaging : JMRI 2014; 39: 276–285

Zhu L, Cheng Q, Luo W, Bao L, Guo G. A comparative study of apparent diffusion coefficient and intravoxel incoherent motion-derived parameters for the characterization of common solid hepatic tumors. Acta radiologica (Stockholm, Sweden : 1987) 2015; 56: 1411–1418

2. Publications

2.1 1st publication

www.nature.com/scientificreports

scientific reports

Check for updates

OPEN

Comparison of different ROI analysis methods for liver lesion characterization with simplified intravoxel incoherent motion (IVIM)

Narine Mesropyan[1,4], Petra Mürtz[1,4], Alois M. Sprinkart[1], Wolfgang Block[1,2,3], Julian A. Luetkens[1], Ulrike Attenberger[1] & Claus C. Pieper[1]✉

This study investigated the impact of different ROI placement and analysis methods on the diagnostic performance of simplified IVIM-DWI for differentiating liver lesions. 1.5/3.0-T DWI data from a respiratory-gated MRI sequence (b = 0, 50, 250, 800 s/mm²) were analyzed in patients with malignant (n = 74/54) and benign (n = 35/19) lesions. Apparent diffusion coefficient ADC = ADC(0,800) and IVIM parameters $D_1' = ADC(50,800)$, $D_2' = ADC(250,800)$, $f_1' = f(0,50,800)$, $f_2' = f(0,250,800)$, and $D^{*\prime} = D^*(0,50,250,800)$ were calculated voxel-wise. For each lesion, a representative 2D-ROI, a 3D-ROI whole lesion, and a 3D-ROI from "good" slices were placed, including and excluding centrally deviating areas (CDA) if present, and analyzed with various histogram metrics. The diagnostic performance of 2D- and 3D-ROIs was not significantly different; e.g. AUC ($ADC/D_1'/f_1'$) were 0.958/0.902/0.622 for 2D- and 0.942/0.892/0.712 for whole lesion 3D-ROIs excluding CDA at 1.5 T ($p > 0.05$). For 2D- and 3D-ROIs, AUC ($ADC/D_1'/D_2'$) were significantly higher, when CDA were excluded. With CDA included, AUC ($ADC/D_1'/D_2'/f_1'/D^{*\prime}$) improved when low percentiles were used instead of averages, and was then comparable to the results of average ROI analysis excluding CDA. For lesion differentiation the use of a representative 2D-ROI is sufficient. CDA should be excluded from ROIs by hand or automatically using low percentiles of diffusion coefficients.

Diffusion-weighted imaging (DWI) is one of the most promising non-contrast techniques that can be readily implemented in standard liver magnetic resonance imaging (MRI) examinations allowing for lesion detection and differentiation[1]. In routine clinical practice the apparent diffusion coefficient (ADC) is usually calculated with b-values between 0 and 500–1000 s/mm² assuming a mono-exponential relationship between signal intensity and the b-value[2]. However the ADC is not only influenced by molecular diffusion, but also by other (pseudo) random motion such as blood flow in small vessels within the tissue (perfusion). According to the intravoxel incoherent motion (IVIM) theory, diffusion and perfusion effects can be separated assuming a bi-exponential behavior of signal intensity, ultimately yielding the diffusion coefficient D, the pseudo-diffusion coefficient D* and the perfusion fraction f[3–7]. f is associated with microvessel density[8,9]. D* was negatively correlated with the interstitial fluid pressure (IFP), which influences blood flow[10]. The problems with IVIM in clinical liver MRI are long acquisition times and limited data quality caused by respiratory and cardiac motion and by low signal-to-noise ratio, which may lead to unstable fitting results, measurement errors and poor reproducibility[11–14]. Improved stability can be achieved by segmented fitting approaches, which decrease the degree of freedom by determining the parameters step by step[15–19] or by simplified IVIM, which uses numerically stable computation of IVIM parameter estimations from 4 b-values[20–27].

For quantitative analysis of ADC and IVIM parameter maps in lesions a region of interest (ROI) based approach is the most commonly used[28–30]. However, there are different ROI-placement and analysis strategies,

[1]Department of Diagnostic and Interventional Radiology, University Hospital Bonn, Venusberg-Campus 1, 53127 Bonn, Germany. [2]Department of Radiotherapy and Radiation Oncology, University Hospital Bonn, Venusberg-Campus 1, 53127 Bonn, Germany. [3]Department of Neuroradiology, University Hospital Bonn, Venusberg-Campus 1, 53127 Bonn, Germany. [4]These authors contributed equally: Narine Mesropyan and Petra Mürtz. ✉email: claus_christian.pieper@ukbonn.de

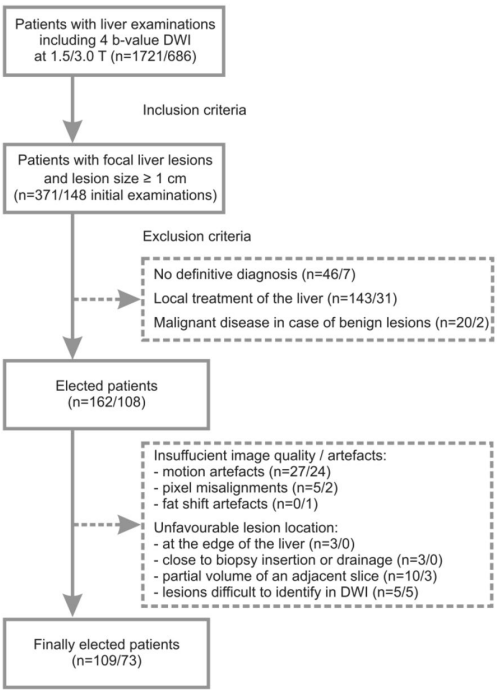

Figure 1. Flow chart of inclusion and exclusion criteria of the study sample.

Patients	3.0 T				1.5 T			
	Total number	Number of males	Age (MV ± SD) [years]	Age range [years]	Total number	Number of males	Age (MV ± SD) [years]	Age range [years]
HCC	26	23	69 ± 10	50–87	32	20	71 ± 9	55–87
CCC	5	3	72 ± 3	68–76	8	4	69 ± 10	57–85
CRC	13	8	63 ± 8	52–81	22	17	60 ± 10	47–87
BC	10	0	57 ± 9	45–72	12	0	60 ± 6	48–70
Hemangioma	11	5	46 ± 13	32–72	23	12	51 ± 14	34–84
FNH	8	0	37 ± 11	22–49	12	1	37 ± 13	14–54

Table 1. Group composition and demographic data of included subjects at 3.0 and 1.5 T. MV—mean value, SD—standard deviation, HCC—hepatocellular carcinoma, CCC—cholangiocellular carcinoma, CRC—metastases of colorectal carcinoma, BC—metastases of breast cancer, FNH—focal nodular hyperplasia.

mostly only investigated for ADC: to place the ROIs into areas with most restricted diffusion ("hot spots", focused ROIs), to average over multiple small ROIs placed into different regions, to place a large ROI on a central slice of a lesion, or to cover the whole lesion[7,21,23]. Usually ROI-analysis is done by averaging the voxel values within the ROI (mean). However, in order to address tumor heterogeneity, also histogram-based approaches are employed to subclassify different tumor diffusion and perfusion environments[7,31].

The purpose of this study was to investigate whether there are differences in the diagnostic accuracy of ADC and IVIM parameters in the discrimination of liver lesions using different ROI placement and analysis strategies. We compared 2D- and 3D-volume ROIs, inclusion and exclusion of central necrosis, cystic components and scars, and ROI analysis by averaging and histogram metrics.

Materials and methods

Study cohort. This single-center retrospective study was approved by the ethics committee of the University Hospital of the Rheinische Friedrich-Wilhelms University Bonn, Germany, with a waiver for written informed consent. Data of consecutive patients with focal hepatic lesions ≥ 1 cm undergoing clinical MRI examination of the liver including 4 b-value DWI from 2013 to 2016 were used. A flowchart of patient inclusion and exclusion is given in Fig. 1. Finally, data of 109/73 patients at 1.5/3.0 T were analyzed (Table 1). These two patient groups had

Name	Value at 3.0 T	Value at 1.5 T
FOV (RLxAP)/orientation	400 × 352 mm/transversal	380 × 326 mm/transversal
Slice number/thickness/gap	26/7.0 mm/0.7 mm	30/7.0 mm/0.7 mm
Matrix/resolution	132 × 113/3.0 × 3.1 mm	112 × 94/3.4 × 3.5 mm
Echo time (TE)	44 ms	63 ms
Repetition time (TR)	1 respiratory cycle	1 respiratory cycle
Imaging time per respiration	1894 ms	1600 ms
EPI-/half-Fourier-/SENSE-factor	41/0.6/3	51/0.6/2
Diffusion gradients	3 orthogonal directions	3 orthogonal directions
b-values (number of averages per direction)	0, 50, 250 s/mm² (NSA = 2), 800 s/mm² (NSA = 4)	0, 50, 250 s/mm² (NSA = 2), 800 s/mm² (NSA = 4)
Fat suppression methods	SPIR + SSGR	SPIR
Water-fat shift/BW	11.1 Pixel/39.0 Hz	9.2 Pixel/23.6 Hz
BW in EPI frequency direction	3346.0 Hz	1437.9 Hz
Acquisition time	Around 4 min (2:42 min without gating)	Around 4 min (2:42 min without gating)

Table 2. Parameters of the diffusion-weighted imaging (DWI) sequence. SENSE—parallel imaging with sensitivity encoding, FOV—field of view, RL—right-left, AP—anterior–posterior, EPI—echo-planar imaging, SPIR—spectral presaturation by inversion recovery, SSGR—slice-selective gradient reversal (uses slice-selection gradients of opposite polarity for the 180° pulses taking advantage of the chemical shift of fat with respect to water), BW—bandwidth.

already been examined in previous studies[21,23]. In those studies basic investigations concerning simplified IVIM for liver lesion characterization had been performed. In the present study, the data were used to investigate the influence of different ROI placement and analysis methods concerning diagnostic accuracy.

Diagnosis of liver lesions was undertaken within clinical routine. Cholangiocellular carcinomas (CCCs) were histologically proven. Hepatocellular carcinomas (HCCs) were either histologically proven or diagnosed according to the American Association for the Study for Liver Disease MRI criteria[32]. Diagnosis of metastasis was based on typical imaging features in combination with histologically proven primary cancer. Diagnosis of focal nodular hyperplasia (FNH) or haemangioma was established on the basis of typical radiological findings on contrast-enhanced MRI and was confirmed by at least one follow-up examination.

Magnetic resonance imaging. Imaging was performed on clinical whole-body 1.5/3.0-T MRI systems (Ingenia, Philips Healthcare; 1.5/3.0-T gradient system: 45/45 mT/m maximum amplitude, 200/200 T/m/s maximum slew rate; 3.0-T system with dual source RF transmission) using 32-channel abdominal coils with a digital interface for signal reception. The standardized imaging protocol included a DWI sequence with a respiratory-triggered single-shot spin-echo echo-planar imaging variant with four b-values (0, 50, 250, 800 s/mm²) before contrast agent administration (Table 2). For each slice, an isotropic diffusion-weighted image was reconstructed from the three images obtained for the different diffusion directions.

Postprocessing. As described previously[21,23], two different approximations of D and f were calculated from signal intensities S(b) and S(0) of the acquired b-values, one from $b_0 = 0$, $b_1 = 50$, $b_3 = 800$ and one from $b_0 = 0$, $b_2 = 250$, $b_3 = 800$ s/mm²:

$$D_1' = ADC(50, 800) = \frac{\ln(S(b_1)) - \ln(S(b_3))}{b_3 - b_1} \tag{1}$$

$$D_2' = ADC(250, 800) = \frac{\ln(S(b_2)) - \ln(S(b_3))}{b_3 - b_2} \tag{2}$$

$$f_1' = f(0, 50, 800) = 1 - \frac{S(b_1)}{S(0)} \cdot \exp^{D_1' \cdot b_1} \tag{3}$$

$$f_2' = f(0, 250, 800) = 1 - \frac{S(b_2)}{S(0)} \cdot \exp^{D_2' \cdot b_2} \tag{4}$$

From the four b-values, D* was approximated by using D_2' and f_2' and the reading for b_1:

$$D^{*\prime} = D^*(0, 50, 250, 800) = -\frac{1}{b_1} \cdot \ln\left[\frac{1}{f_2'} \cdot \left(\frac{S(b_1)}{S(0)} - \left(1 - f_2'\right) \cdot \exp^{-D_2' \cdot b_1}\right)\right] \tag{5}$$

D*′ cannot be determined for all voxels, because some voxels are not affected by perfusion. Voxels with not defined values were excluded from ROI analysis.

Moreover, the conventional ADC was calculated:

$$ADC = ADC(0, 800) = \frac{\ln(S(b_0)) - \ln(S(b_3))}{b_3 - b_0} \quad (6)$$

Parameter maps and ROI analyses were calculated offline using custom written software in MATLAB (MathWorks, Natick, MA).

Image analysis. Image analysis was performed by a radiologist (N.M.) with 3 years of experience and checked by a radiologist (C.C.P.) with 10 years of experience in abdominal imaging and a physicist (P.M.) with more than 20 years of experience in DWI. All were blinded to clinical information.

One reference lesion per lesion type was analyzed. For each included lesion, 2D- and 3D-volume ROI-based analyses were performed. ROIs were placed as large as possible using DWI with highest contrast between lesion and normal tissue and excluding areas close to the lesion rim to avoid partial-volume effects. After the anatomical position of each ROI had been visually cross-checked for pixel misalignments between images with different b-values, the ROI was analyzed in the related parameter maps.

For 2D-analysis, one hand-drawn ROI was placed centrally in each lesion on a single representative slice (reference slice), which was largely unaffected by motion and susceptibility artifacts and pixel misalignments. For the 3D-volume analysis, a hand-drawn ROI was placed on each slice of the lesion. Slices with artifacts and pixel misalignments as well as the first and the last slice (due to potential partial volume effect) were marked as "bad". An example of ROI placement is given in Fig. 2. Data from all slices ("good" and "bad") were combined into a whole-lesion 3D-volume ROI (3DA). Furthermore, a second 3D-volume ROI was calculated including only the "good" slices (3DG). Thus, in each lesion three different ROI-sizes were investigated (2D, 3DA, 3DG).

For lesions with central necrosis, cystic components or scars (centrally deviating areas in DWI), the 2D- and 3D-ROI placements were repeated with exclusion of such areas. Two example analyses are given in Fig. 3. These measurements allowed the evaluation of different ROI sizes as well as of different lesion tissues included to the ROIs.

Finally, a histogram analysis was performed for each 2D-ROI. The following histogram metrics were calculated: median, standard deviation, the 5th, 10th, 25th, 75th, 90th, 95th percentiles, skewness and kurtosis.

Statistical analysis. Statistical analysis was performed using SPSS (Version 24.0, IBM) and pROC package (Version 1.16.2) in R (Version 3.6.1)[33]. Receiver operating characteristic (ROC) analysis was performed for liver lesions discrimination. Youden's index was used to determine the optimal cut-off of the ROC curve providing the best trade-off between sensitivity and specificity. DeLong method was used to compare dependent ROC curves[34]. The area under the curve (AUC) based on mean ROI values was compared for the different ROI variants. Furthermore, it was investigated, whether AUC values can be improved by using one of the histogram metrics instead of the mean value. These investigations were carried out for both types of ROIs, including and excluding centrally deviating areas. In order to investigate whether histogram analyses may replace manual exclusion of such areas, additionally a comparison was performed using ROIs excluding such areas in case of mean values and including them in case of histogram metrics.

Ethical approval and informed consent. The presented study was approved by the institutional review board of the University of Bonn and hence all methods were performed in compliance with the ethical standards set in the 1964 Declaration of Helsinki as well as its later amendments. Written informed consent was waived.

Results

At 1.5/3.0 T, 74/54 malignant and 35/19 benign liver lesions were analyzed (Table 1). Mean volume of malignant lesions was 96.6/76.6 cm^3 (range: 1.3–1715.7/1.2–521.2 cm^3) and of benign lesions 72.1/20.4 cm^3 (range: 0.9–856.3/1.1–118.3 cm^3). Of these 109/73 lesions, 36/11 had centrally deviating areas. In total, 1333 ROIs were placed. The mean values of ADC and IVIM parameters for the benign and malignant lesion group together with the ROC analyses results for lesion differentiation are presented in Table 3. In Fig. 4 an overview to the obtained AUC values are given. In general, the values of diffusion and perfusion sensitive parameters were lower in malignant lesions than in benign lesions.

The highest AUC values for lesion differentiation were found for ADC (0.967–0.911) and D_1' (0.941–0.857) followed by D_2' (0.919–0.816), f_2' (0.731–0.656), f_1' (0.673–0.616), and $D^{*\prime}$ (0.563–0.515). For all parameters, diagnostic performance was compared for the different 2D- and 3D-ROI variants, for ROIs in- and excluding centrally deviating areas, and for mean values and histogram metrics.

Comparison of 2D- and 3D-ROIs. In Table 4 the results of the AUC value comparisons with respect to the different ROI types (2D, 3DG, 3DA) are presented. No significant differences were found in any of the comparisons, neither for ROIs that include centrally deviating areas, nor for those excluding such areas. The only exceptions were that AUC values for 3DA ROIs compared to those for 3DG ROIs were slightly larger in case of f_1' and f_2' at 1.5 T (for ROIs including centrally deviating areas: 0.712 vs 0.620 with $p = 0.049$ and 0.761 vs 0.675 with $p = 0.031$, respectively; for ROIs excluding those areas: 0.712 vs 0.622 with $p = 0.055$ and 0.773 vs 0.688 with $p = 0.029$, respectively), and in case of D_2' at 3.0 T, but only for ROIs including centrally deviating areas (0.895 vs 0.825 with $p = 0.029$).

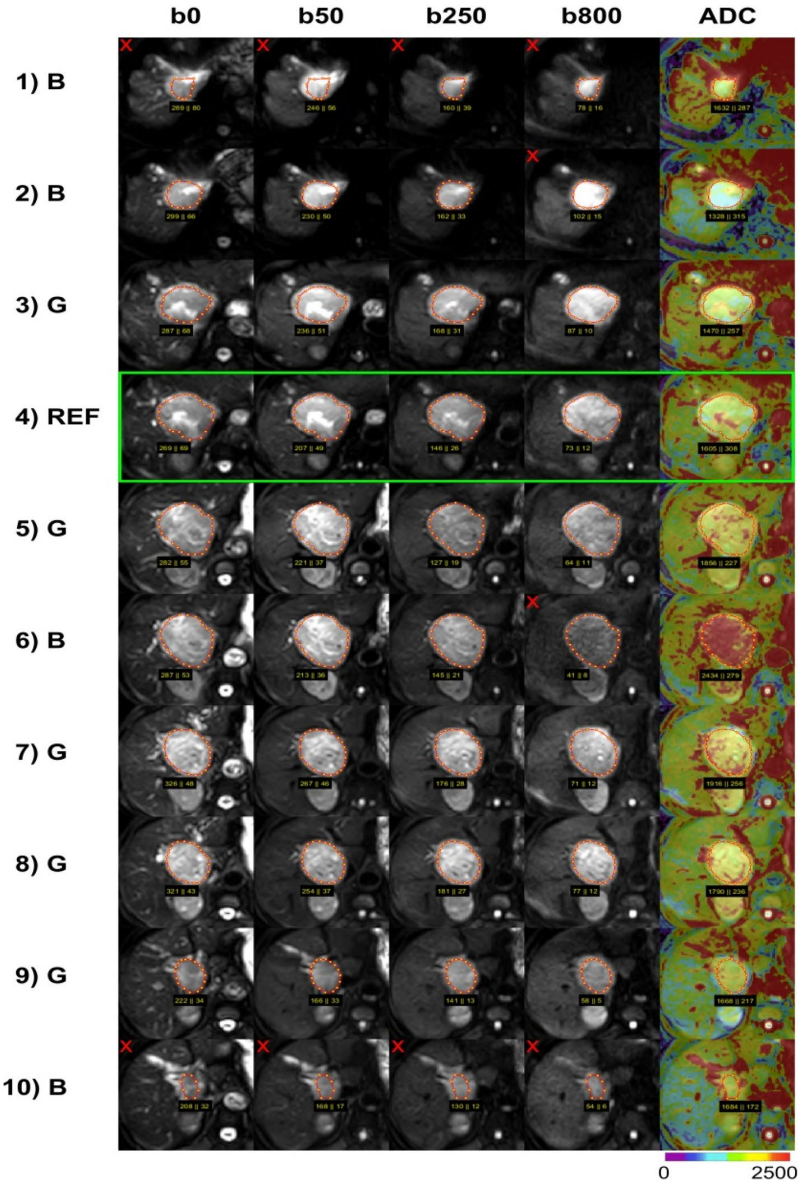

Figure 2. A typical example of 2D and 3D DWI IVIM analysis in a hepatocellular carcinoma at 1.5 T. Original diffusion-weighted images with b = 0, 50, 250, 800 s/mm^2 are presented together with conventional ADC maps displayed as color-coded overlays over b800 images. For analysis, on each tumor-containing slice a region of interest (ROI) was selected, where ADC and IVIM parameters (not shown) were analyzed. ADC values are given in units of 10^{-6} mm^2/s. Slices largely unaffected by artifacts were defined as good ("G"), slices close to the lesion's rim (partial volume) or with images affected by artifacts (see red x) due to motion, susceptibility or pixel misalignments were defined as bad ("B"). One central "good" slice served as reference ("REF") for the 2D analysis (see green frame), hereby slices in the lower part of the liver should be preferred due to lower motion influences from the heart. For 3D analysis, the voxels of the 2D ROI were combined with voxels of the ROIs on other "good" slices (3DG), voxels of all ROIs was used for whole lesion analysis (3DA).

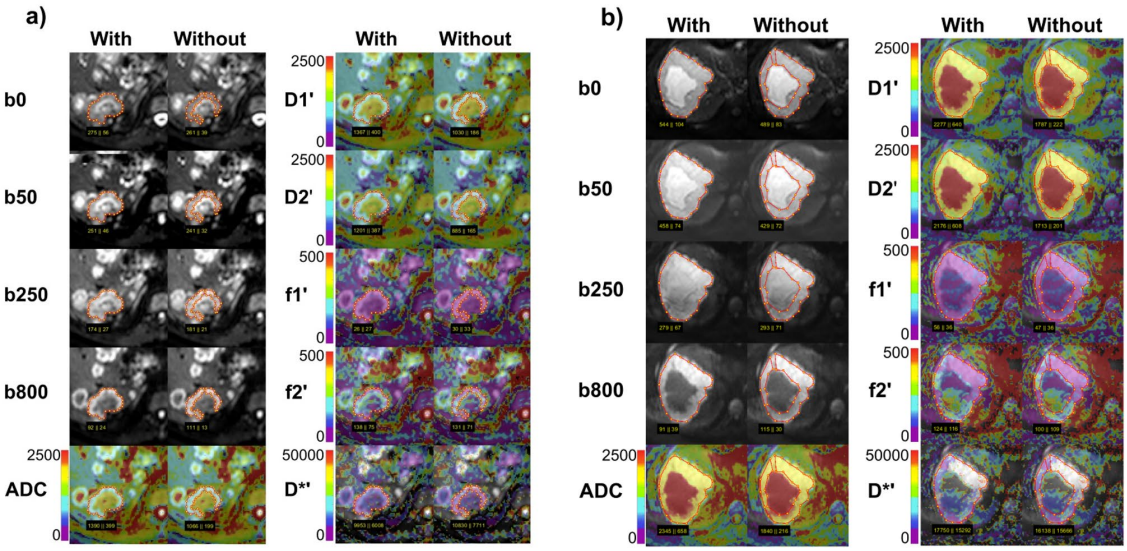

Figure 3. Typical examples of DWI IVIM analysis comparing in- and exclusion of necrosis in a metastasis of colorectal carcinoma (**a**) and of liquid in a hemangioma (**b**) at 1.5 T. For one central slice per lesion, original diffusion-weighted images with b = 0, 50, 250, 800 s/mm^2 are presented together with conventional ADC, diffusion sensitive D_1' and D_2' parameter maps, and perfusion sensitive f_1', f_2', $D^{*\prime}$ parameter maps. The parameter maps are displayed as color-coded overlays over b = 800. Values of ADC, D_1', D_2' and $D^{*\prime}$ are given in units of 10^{-6} mm^2/s, those of f_1' and f_2' in 10^{-3}. If bad data quality led to negative parameter values or to not defined values, these voxels were not colorized. When necrosis/cystic components were excluded ("Without") from regions of interests (ROIs), the diffusion sensitive parameters were significantly lower compared to inclusion ("With"). Perfusion sensitive parameters remained unchanged because there is only low perfusion in the metastasis and hemangioma anyway.

Comparison of ROIs with included and excluded central necrosis, cystic components or scars. Table 5 summarizes the results of AUC value comparison with respect to included tissue. Exclusion of centrally deviating areas from ROIs yields larger AUC values of ADC, D_1', and D_2', for all 2D- and 3D-ROI variants. Improvements were significant at 1.5 T, at 3 T, however, sometimes only by tendency, potentially due to fewer cases with centrally deviating areas. For 2D-ROIs at 1.5 T for example, AUC values of ADC improved from 0.925 to 0.958 ($p = 0.01$), of D_1' from 0.866 to 0.902 ($p = 0.0081$), and of D_2' from 0.822 to 0.864 (0.00089). Perfusion parameters did not show any differences. Typical examples of DWI IVIM analysis comparing in- and exclusion of centrally deviating areas are presented in Fig. 3.

Comparison of mean values versus histogram analysis. Table S1 gives the mean values and values of histogram metrics for the benign and malignant lesion group together with the ROC analyses results for lesion differentiation using 2D-ROIs. In Table S2 the results of the different AUC value comparisons are given.

At 1.5 T, the 5th and 10th percentiles of ADC and D_1' and the 25th percentiles of ADC, D_1' and D_2' lead to significantly higher AUC values than the mean values for ROIs including centrally deviating areas. For example, by using the 10th percentile instead of mean value, AUC values could be improved for ADC from 0.925 to 0.969 ($p = 0.018$), for D_1' from 0.866 to 0.926 ($p = 0.0042$), and for D_2' from 0.822 to 0.856 ($p = 0.074$). For ROIs excluding centrally deviating areas, these improvements were observed to a lesser degree. For example, by using the 10th percentile instead of mean value, AUC values could only be improved for ADC from 0.958 to 0.975 ($p = 0.13$) and for D_1' from 0.902 to 0.935 ($p = 0.038$) and not for D_2'. The additional comparison using ROIs excluding centrally deviating areas in case of mean value analysis and including such areas in case of histogram analysis, no significant differences were found for ADC, D_1' and D_2'. This means, that the use of low percentiles can replace the elaborate exclusion of centrally deviating areas by hand without reducing the diagnostic accuracy. At 3.0 T, where there were fewer cases with centrally deviating areas, similar results were obtained but with higher *p*-values.

At both field strengths, the 5th and 10th percentiles of $D^{*\prime}$ lead to significantly higher AUC values than the mean values, regardless of whether centrally deviating areas were included or excluded or excluded only in case of mean value analysis. For example, by using the 5th percentile instead of the mean value, AUC values could be improved from 0.515 to 0.646 ($p = 0.00085$) at 1.5 T and from 0.559 to 0.717 ($p = 0.0079$) at 3.0 T for ROIs excluding centrally deviating areas. This behavior also tended to be observed for f_1'. For example, by using the 5th percentile instead of the mean value, AUC values could be improved from 0.622 to 0.708 ($p = 0.034$) at 1.5 T and from 0.661 to 0.681 ($p = 0.74$) at 3.0 T for ROIs excluding centrally deviating areas. All other histogram metrics

ROI	Par	Malignant			Benign			Dir	AUC	CI1	CI2	Cut-off	Sen	Spec	Acc
		MV	SD	N	MV	SD	N								
(a) 1.5 T															
ROIs including centrally deviating areas															
2D	ADC	1182	216	74	1712	329	35	>	0.925	0.878	0.972	1335.8	0.797	0.914	0.835
	D_1'	1115	224	74	1600	401	35	>	0.866	0.796	0.935	1130.4	0.622	0.943	0.725
	D_2'	990	280	74	1442	433	35	>	0.822	0.733	0.911	1105.0	0.689	0.857	0.743
	f_1'	64	31	74	97	70	35	>	0.621	0.490	0.753	110.7	0.905	0.457	0.761
	f_2'	145	96	74	191	104	35	>	0.656	0.546	0.766	198.9	0.838	0.429	0.706
	$D^{*\prime}$	18,370	8332	74	21,200	13,245	35	>	0.529	0.401	0.656	25,008.0	0.811	0.371	0.670
3DG	ADC	1202	223	74	1731	356	35	>	0.914	0.863	0.966	1311.7	0.730	0.943	0.798
	D_1'	1129	226	74	1616	401	35	>	0.860	0.787	0.933	1431.5	0.919	0.657	0.835
	D_2'	1020	253	74	1467	436	35	>	0.828	0.739	0.917	1183.2	0.797	0.743	0.780
	f_1'	66	29	74	99	63	35	>	0.620	0.490	0.751	106.5	0.932	0.457	0.780
	f_2'	139	68	74	192	97	35	>	0.675	0.566	0.785	183.5	0.838	0.457	0.716
	$D^{*\prime}$	17,436	5452	74	19,242	8748	35	>	0.542	0.410	0.675	24,886.1	0.932	0.371	0.752
3DA	ADC	1230	234	74	1748	329	35	>	0.911	0.859	0.963	1498.4	0.892	0.771	0.853
	D_1'	1147	235	74	1607	360	35	>	0.857	0.783	0.932	1468.4	0.919	0.686	0.844
	D_2'	1057	246	74	1466	375	35	>	0.824	0.730	0.917	1206.9	0.824	0.771	0.807
	f_1'	73	29	74	115	56	35	>	0.712	0.595	0.830	117.3	0.932	0.514	0.798
	f_2'	135	55	74	202	87	35	>	0.761	0.662	0.859	172.4	0.851	0.657	0.789
	$D^{*\prime}$	18,120	4533	74	19,437	7967	35	>	0.536	0.401	0.672	24,541.3	0.946	0.343	0.752
ROIs excluding centrally deviating areas															
2D	ADC	1124	180	74	1692	313	35	>	0.958	0.922	0.993	1338.5	0.892	0.914	0.899
	D_1'	1057	188	74	1580	387	35	>	0.902	0.842	0.962	1173.6	0.757	0.886	0.798
	D_2'	939	250	74	1423	416	35	>	0.864	0.783	0.946	1142.5	0.838	0.829	0.835
	f_1'	63	31	74	97	70	35	>	0.622	0.491	0.754	114.5	0.932	0.457	0.780
	f_2'	141	96	74	191	104	35	>	0.672	0.563	0.781	140.0	0.622	0.657	0.633
	$D^{*\prime}$	18,837	8603	74	21,189	13,251	35	>	0.515	0.388	0.642	24,996.2	0.784	0.371	0.651
3DG	ADC	1144	187	74	1717	357	35	>	0.949	0.911	0.987	1310.2	0.838	0.943	0.872
	D_1'	1072	194	74	1602	399	35	>	0.894	0.831	0.957	1333.0	0.946	0.714	0.872
	D_2'	966	215	74	1454	432	35	>	0.866	0.783	0.948	1179.3	0.892	0.743	0.844
	f_1'	66	29	74	99	63	35	>	0.622	0.491	0.752	106.8	0.932	0.457	0.780
	f_2'	137	66	74	192	97	35	>	0.688	0.580	0.797	149.9	0.703	0.629	0.679
	$D^{*\prime}$	17,634	5757	74	19,225	8735	35	>	0.535	0.404	0.665	24,616.8	0.905	0.371	0.734
3DA	ADC	1176	201	74	1736	330	35	>	0.942	0.902	0.983	1447.8	0.932	0.800	0.890
	D_1'	1094	203	74	1594	357	35	>	0.892	0.828	0.956	1314.9	0.905	0.743	0.853
	D_2'	1006	211	74	1454	371	35	>	0.853	0.764	0.941	1314.9	0.946	0.714	0.872
	f_1'	73	30	74	115	56	35	>	0.712	0.594	0.829	116.9	0.919	0.514	0.789
	f_2'	134	55	74	202	87	35	>	0.773	0.677	0.869	172.2	0.865	0.657	0.798
	$D^{*\prime}$	18,277	4901	74	19,381	7927	35	>	0.530	0.396	0.665	24,767.8	0.932	0.343	0.743
(b) 3.0 T															
ROIs including centrally deviating areas															
2D	ADC	1120	183	54	1566	251	19	>	0.931	0.858	1.000	1419.4	0.963	0.789	0.918
	D_1'	1062	175	54	1463	278	19	>	0.893	0.803	0.983	1292.6	0.926	0.737	0.877
	D_2'	976	189	54	1310	318	19	>	0.816	0.699	0.932	1183.8	0.870	0.632	0.808
	f_1'	59	39	54	98	66	19	>	0.662	0.494	0.830	96.6	0.870	0.526	0.781
	f_2'	118	76	54	188	118	19	>	0.667	0.501	0.832	172.1	0.833	0.579	0.767
	$D^{*\prime}$	17,273	7256	53	19,740	10,820	17	>	0.563	0.389	0.736	21,309.9	0.774	0.412	0.686
3DG	ADC	1138	181	54	1549	224	19	>	0.933	0.862	1.000	1420.9	0.963	0.789	0.918
	D_1'	1081	175	54	1477	229	19	>	0.918	0.841	0.995	1392.7	0.981	0.737	0.918
	D_2'	1000	166	54	1328	307	19	>	0.825	0.708	0.941	1345.9	1.000	0.526	0.877
	f_1'	63	39	54	92	64	19	>	0.616	0.452	0.780	125.4	0.944	0.368	0.795
	f_2'	118	52	54	183	116	19	>	0.668	0.493	0.842	180.0	0.852	0.526	0.767
	$D^{*\prime}$	17,477	6597	54	19,055	10,602	18	>	0.528	0.358	0.697	34,209.4	0.981	0.167	0.778

Continued

ROI	Par	Malignant			Benign			Dir	AUC	CI1	CI2	Cut-off	Sen	Spec	Acc
		MV	SD	N	MV	SD	N								
3DA	ADC	1148	173	54	1578	209	19	>	0.952	0.893	1.000	1391.4	0.944	0.895	0.932
	D_1'	1088	168	54	1489	223	19	>	0.922	0.845	0.999	1383.9	0.981	0.789	0.932
	D_2'	1016	159	54	1358	241	19	>	0.895	0.820	0.970	1067.5	0.630	1.000	0.726
	f_1'	66	39	54	96	46	19	>	0.673	0.526	0.819	83.5	0.759	0.579	0.712
	f_2'	119	55	54	179	81	19	>	0.728	0.593	0.863	125.8	0.648	0.789	0.685
	$D^{*\prime}$	17,457	5301	54	17,501	8499	19	<	0.522	0.362	0.683	17,598.3	0.537	0.632	0.562
ROIs excluding centrally deviating areas															
2D	ADC	1090	167	54	1566	251	19	>	0.953	0.891	1.000	1276.1	0.870	0.947	0.890
	D_1'	1032	156	54	1463	278	19	>	0.920	0.843	0.997	1214.9	0.944	0.789	0.904
	D_2'	945	171	54	1310	318	19	>	0.852	0.747	0.957	1183.8	0.963	0.632	0.877
	f_1'	59	38	54	98	66	19	>	0.661	0.493	0.829	96.6	0.870	0.526	0.781
	f_2'	119	76	54	188	118	19	>	0.666	0.499	0.832	172.1	0.833	0.579	0.767
	$D^{*\prime}$	17,895	8443	54	19,740	10,820	17	>	0.559	0.388	0.730	21,309.9	0.759	0.412	0.676
3DG	ADC	1110	163	54	1549	224	19	>	0.951	0.887	1.000	1283.1	0.852	0.947	0.877
	D_1'	1053	156	54	1477	229	19	>	0.936	0.867	1.000	1334.1	1.000	0.789	0.945
	D_2'	974	149	54	1328	307	19	>	0.853	0.745	0.961	1182.9	0.926	0.632	0.849
	f_1'	63	39	54	92	64	19	>	0.620	0.458	0.782	125.4	0.944	0.368	0.795
	f_2'	118	52	54	183	116	19	>	0.667	0.492	0.841	178.1	0.852	0.526	0.767
	$D^{*\prime}$	17,301	6543	54	19,055	10,602	18	>	0.538	0.370	0.707	16,348.6	0.500	0.667	0.542
3DA	ADC	1125	160	54	1578	209	19	>	0.967	0.914	1.000	1386.6	0.981	0.895	0.959
	D_1'	1065	154	54	1489	223	19	>	0.941	0.877	1.000	1367.4	1.000	0.789	0.945
	D_2'	995	150	54	1358	241	19	>	0.919	0.857	0.982	1067.5	0.704	1.000	0.781
	f_1'	67	39	54	96	46	19	>	0.673	0.527	0.818	116.1	0.907	0.421	0.781
	f_2'	118	54	54	179	81	19	>	0.731	0.596	0.866	126.7	0.648	0.789	0.685
	$D^{*\prime}$	17,394	5200	54	17,501	8499	19	<	0.517	0.356	0.677	17,598.3	0.519	0.632	0.548

Table 3. Results of ADC and IVIM parameter value analysis within different regions of interest (ROIs) and receiver operating characteristic (ROC) analysis of benign and malignant liver lesions. ADC, D_1', D_2', D*' values are given in units of 10^{-6} mm^2/s, f_1' and f_2' values are given in units of 10^{-3}.

including skewness and kurtosis performed with lower or not significantly different AUC values compared to the ROI mean values.

Discussion

The main findings of the present study were: (1) No significant differences in diagnostic performance were found between 2D- and 3D-ROIs even if only slices with good image quality were included. (2) Differentiation was more accurate when centrally deviating areas were excluded from ROIs. (3) When such areas were included, diagnostic accuracy of diffusion sensitive parameters was improved by histogram analysis of the ROIs using low percentiles instead of mean values. (4) Diagnostic accuracy of perfusion parameters, especially of $D^{*\prime}$ was improved by histogram analysis using low percentiles instead of mean values, regardless of whether centrally deviating areas were in- or excluded.

To our knowledge, to date no systematic evaluation of different ROI placement and analysis methods for liver lesion analysis by IVIM-derived DWI parameters has been performed. However, it is important for potential clinical use of IVIM DWI techniques for lesion characterization to establish an appropriate ROI placement and analysis strategy as simple as possible that leads to highest possible diagnostic accuracy.

The technically simplest way for ROI placement in clinical practice is to draw a single 2D-ROI on a representative slice encompassing the whole lesion including centrally deviating areas. In scientific studies, however, 3D-volume ROIs are often used e.g. together with automated segmentation software. In the present work we performed comparisons with respect to ROI-type (2D on a reference slice, 3DA for whole-tumor volume, 3DG considering only "good" slices) and tumor tissue by inclusion and exclusion of centrally deviating areas. For different ROI-types, we did not find significant differences in diagnostic accuracy of ADC and IVIM parameters. Compared to 3D-whole-lesion ROIs (3DA), the inclusion of only "good" slices (3DG) or the selection of a ROI on a reference slice (2D) was expected to improve diagnostic accuracy due to less influence of artifacts, pixel misalignments and partial volume effects. However, this effect was hard to find. One reason might be that in case of whole-tumor 3DA volumes negative influences by "bad" slices were compensated by improved statistics due to higher number of included voxels compared to 3DG and 2D. More voxel averaging and thus a better noise robustness was noticeable especially in small lesions (see Table S3). A previous study on prostate cancer also yielded no improved diagnostic performance using 3D-ROIs instead of 2D-ROIs[35]. Although further studies on a larger population with liver lesions are needed to confirm the finding of this study, the analysis of a central

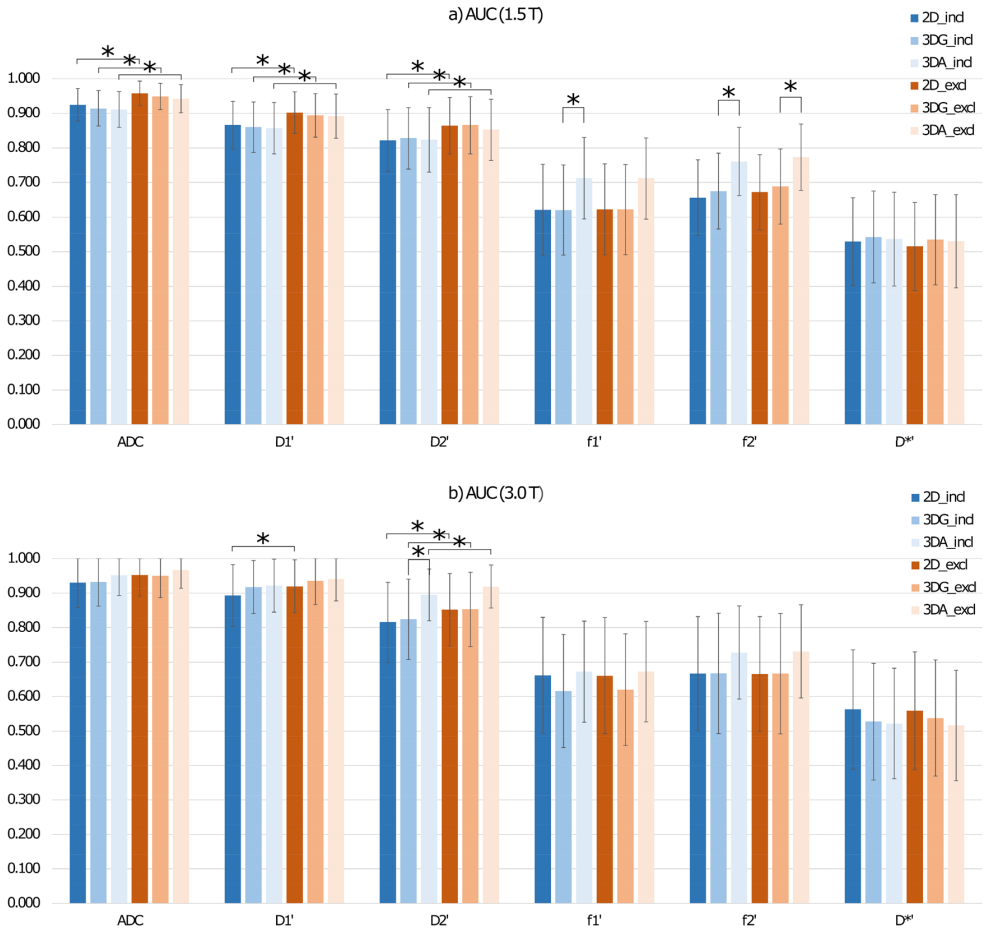

Figure 4. Overview to obtained AUC values (**a**) at 1.5 T and (**b**) at 3.0 T for the different ROIs (2D, 3DG, 3DA) and with included and excluded central necrosis, cystic components or scars. Significant differences are marked by "*".

representative slice of "good" image quality seems to be sufficient for reliable lesion discrimination and is applicable in clinical practice and less time consuming.

The exclusion of centrally deviating areas significantly improves the diagnostic accuracy of diffusion parameters, as was to be expected. For perfusion parameters no differences were found. A previous study on breast lesions, also found improved accuracy of differential diagnosis for ADC in ROIs including only viable tissue instead of whole tumor[29]. Necrosis, cystic areas and scars increase the diffusion coefficient of a lesion at random due to the admixture of varied proportions of high values. Especially in case of necrosis, the malignancy of tumors may be masked by measurement of a higher ADC due to varying amounts of necrotic tissue. Perfusion parameters, in contrast, are low in necrosis which further reduces the already small values in malignant tumors. In liver metastases, a correlation was found between diffusion parameters and liver tumor necrosis, but not for perfusion parameters[36].

For lesion assessment, the exclusion of centrally deviating areas is more time consuming and, therefore, not a routine clinical practice and can be challenging for unexperienced radiologists. Thus, automated segmentation would be helpful. In this respect, histogram analysis can provide additional quantitative metrics beyond the mean value of a ROI, which reflect the heterogeneity of pathologic changes without additional imaging[7]. In our study, histogram analysis of ROIs including centrally deviating areas showed that low percentiles led to similar diagnostic accuracy for ADC and diffusion coefficients than mean value analysis of ROIs without such areas. Thus, this method may be of use to automatically determine voxels of viable tumor for ADC and IVIM analysis. In some other studies, it was also shown that diagnostic accuracy of ADC and D in whole-lesion ROI analysis was improved when low percentiles were used instead of mean values, e.g. in predicting microvascular invasion of hepatocellular carcinoma[37], differentiation of malignancy in breast and testicular lesions[31,38], differentiating of different grades of prostate cancer[39], and gliomas[40–42].

Furthermore, of special interest is the finding that for the perfusion parameters, especially D*, diagnostic accuracy in lesion discrimination was significantly improved by the use of low percentiles instead of mean values

Par	AUC 2D	AUC 3DG	*P*	AUC 2D	AUC 3DA	*P*	AUC 3DG	AUC 3DA	*P*
(a) 1.5 T									
ROIs including centrally deviating areas									
ADC	0.925	0.914	0.358	0.925	0.911	0.372	0.914	0.911	0.751
D_1'	0.866	0.860	0.696	0.866	0.857	0.631	0.860	0.857	0.783
D_2'	0.822	0.828	0.817	0.822	0.824	0.959	0.828	0.824	0.756
f_1'	0.621	0.620	0.986	0.621	0.712	0.137	0.620	0.712	0.049*
f_2'	0.656	0.675	0.689	0.656	0.761	0.071	0.675	0.761	0.031*
D*′	0.529	0.542	0.724	0.529	0.536	0.877	0.542	0.536	0.861
ROIs excluding centrally deviating areas									
ADC	0.958	0.949	0.291	0.958	0.942	0.224	0.949	0.942	0.394
D_1'	0.902	0.894	0.594	0.902	0.892	0.565	0.894	0.892	0.815
D_2'	0.864	0.866	0.961	0.864	0.853	0.663	0.866	0.853	0.379
f_1'	0.622	0.622	0.986	0.622	0.712	0.143	0.622	0.712	0.055
f_2'	0.672	0.688	0.729	0.672	0.773	0.075	0.688	0.773	0.029*
D*′	0.515	0.535	0.608	0.515	0.530	0.755	0.535	0.530	0.896
(b) 3.0 T									
ROIs including centrally deviating areas									
ADC	0.931	0.933	0.904	0.931	0.952	0.106	0.933	0.952	0.167
D_1'	0.893	0.918	0.267	0.893	0.922	0.223	0.918	0.922	0.715
D_2'	0.816	0.825	0.803	0.816	0.895	0.056	0.825	0.895	0.029*
f_1'	0.662	0.616	0.299	0.662	0.673	0.851	0.616	0.673	0.254
f_2'	0.667	0.668	0.988	0.667	0.728	0.444	0.668	0.728	0.280
D*′	0.563	0.513	0.374	0.563	0.518	0.780	0.528	0.498	0.848
ROIs excluding centrally deviating areas									
ADC	0.953	0.951	0.867	0.953	0.967	0.174	0.951	0.967	0.186
D_1'	0.920	0.936	0.461	0.920	0.941	0.349	0.936	0.941	0.669
D_2'	0.852	0.853	0.975	0.852	0.919	0.100	0.853	0.919	0.059
f_1'	0.661	0.620	0.338	0.661	0.673	0.837	0.620	0.673	0.282
f_2'	0.666	0.667	0.988	0.666	0.731	0.416	0.667	0.731	0.243
D*′	0.559	0.528	0.591	0.559	0.504	0.720	0.538	0.492	0.766

Table 4. Comparison of AUC values of the ROC curves obtained from 2 and 3D ROIs (see Table 2) at 1.5 T (a) and 3.0 T (b). AUC—area under the curve, *marks significant results, *P*—*p*-value.

regardless of whether centrally deviating areas were included or excluded or excluded only in case of mean value analysis. Because D* depends on blood flow velocity and length of microvessel segments[3,4], this may indicate that differences between benign and malignant lesions exist especially for small vessels. Other studies investigating histogram analysis for IVIM perfusion parameters in liver lesions are rare. There is one other study investigating hepatocellular carcinoma with and without microvascular invasion, but no significant differences were found for parameters D* and f, neither for mean values nor for low percentiles[37].

This study has several limitations. First, it was a retrospective study with inherent methodological limitations. For example, due to the lack of raw data, no motion correction of the individual images[43] could be performed before averaging. Second, although the total number of lesions included was relatively large, only common lesion types were analyzed, which may affect the generalizability of the results. Also, there was a relatively small number of patients who underwent MRI examination at 3.0 T MRI system and, therefore, statistical power was lower compared to 1.5 T. We included a typical clinical patient cohort of a large tertiary reference center so that not only large lesions were included. Therefore, a study including more large lesions may show differences between 2D- and 3D-volume measurements. On the other hand, not even tendencies concerning differences of 2D- and 3D-ROIs were found in the present study.

In conclusion, using representative 2D-ROIs seems to be sufficient for reliable liver lesion discrimination in routine clinical practice. Central necrosis, cystic components or scars should be excluded from ROIs either by hand or by computing low percentiles of diffusion coefficients instead of mean values.

Parameter	ROI	AUC(incl)	AUC(excl)	*P*
(a) 1.5 T				
ADC	2D	0.925	0.958	1.0E−02*
	3DG	0.914	0.949	4.8E−03*
	3DA	0.911	0.942	4.8E−03*
D_1'	2D	0.866	0.902	8.1E−03*
	3DG	0.860	0.894	1.1E−03*
	3DA	0.857	0.892	6.8E−04*
D_2'	2D	0.822	0.864	8.9E−04*
	3DG	0.828	0.866	5.6E−04*
	3DA	0.824	0.853	7.4E−04*
f_1'	2D	0.621	0.622	8.6E−01
	3DG	0.620	0.622	7.6E−01
	3DA	0.712	0.712	8.6E−01
f_2'	2D	0.656	0.672	2.2E−01
	3DG	0.675	0.688	9.0E−02
	3DA	0.761	0.773	5.8E−02
D*′	2D	0.529	0.515	1.8E−01
	3DG	0.542	0.535	2.3E−01
	3DA	0.536	0.530	3.6E−01
(b) 3.0 T				
ADC	2D	0.931	0.953	0.068
	3DG	0.933	0.951	0.069
	3DA	0.952	0.967	0.102
D_1'	2D	0.893	0.920	0.026*
	3DG	0.918	0.936	0.069
	3DA	0.922	0.941	0.052
D_2'	2D	0.816	0.852	0.012*
	3DG	0.825	0.853	0.021*
	3DA	0.895	0.919	0.033*
f_1'	2D	0.662	0.661	0.727
	3DG	0.616	0.620	0.505
	3DA	0.673	0.673	1.000
f_2'	2D	0.667	0.666	0.805
	3DG	0.668	0.667	0.816
	3DA	0.728	0.731	0.420
D*′	2D	0.563	0.569	0.199
	3DG	0.528	0.538	0.174
	3DA	0.522	0.517	0.465

Table 5. Comparison of AUC values of the ROC curves obtained from ROIs including (incl) and excluding (excl) centrally deviating areas like necrosis, cystic components or scars (see Table 1) at 1.5 T (a) and 3.0 T (b). AUC—area under the curve. *marks significant results, *P*—*p* value.

Data availability

The datasets generated during and/or analyzed during the current study are available from the corresponding author on reasonable request.

Received: 21 March 2021; Accepted: 8 October 2021
Published online: 23 November 2021

References

1. Shenoy-Bhangle, A., Baliyan, V., Kordbacheh, H., Guimaraes, A. R. & Kambadakone, A. Diffusion weighted magnetic resonance imaging of liver: Principles, clinical applications and recent updates. *World J. Hepatol.* **9**, 1081–1091 (2017).
2. Thoeny, H. C. & Ross, B. D. Predicting and monitoring cancer treatment response with diffusion-weighted MRI. *J. Magn. Reson. Imaging* **32**, 2–16 (2010).
3. Le Bihan, D. *et al.* Separation of diffusion and perfusion in intravoxel incoherent motion MR imaging. *Radiology* **168**, 497–505 (1988).
4. Koh, D. M., Collins, D. J. & Orton, M. R. Intravoxel incoherent motion in body diffusion-weighted MRI: Reality and challenges. *Am. J. Roentgenol.* **196**, 1351–1361 (2011).

5. Koh, D. M. & Collins, D. J. Diffusion-weighted MRI in the body: Applications and challenges in oncology. *Am. J. Roentgenol.* **188**, 1622–1635 (2007).
6. Koh, D. M. Science to practice: Can intravoxel incoherent motion diffusion-weighted MR imaging be used to assess tumor response to antivascular drugs?. *Radiology* **272**, 307–308 (2014).
7. Padhani, A. R. *et al.* Diffusion-weighted magnetic resonance imaging as a cancer biomarker: Consensus and recommendations. *Neoplasia* **11**, 102–125 (2009).
8. Meyer, H.-J. *et al.* Associations between IVIM histogram parameters and histopathology in rectal cancer. *Magn. Reson. Imaging* **77**, 21–27 (2021).
9. Lee, H. J. *et al.* Tumor perfusion-related parameter of diffusion-weighted magnetic resonance imaging: Correlation with histological microvessel density. *Magn. Reson. Med.* **71**, 1554–1558 (2014).
10. Kim, S. *et al.* Interstitial fluid pressure correlates with intravoxel incoherent motion imaging metrics in a mouse mammary carcinoma model. *NMR Biomed.* **25**, 787–794 (2012).
11. Lee, Y. *et al.* Intravoxel incoherent motion diffusion-weighted MR imaging of the liver: Effect of triggering methods on regional variability and measurement repeatability of quantitative parameters. *Radiology* **274**, 405–415 (2015).
12. Cho, G. Y. *et al.* A versatile flow phantom for intravoxel incoherent motion MRI. *Magn. Reson.* **67**, 1710–1720 (2012).
13. Kakite, S. *et al.* Hepatocellular carcinoma: Short-term reproducibility of apparent diffusion coefficient and intravoxel incoherent motion parameters at 3.0T. *J Magn Reson Imaging* **41**, 149–156 (2015).
14. Andreou, A. *et al.* Measurement reproducibility of perfusion fraction and pseudodiffusion coefficient derived by intravoxel incoherent motion diffusion-weighted MR imaging in normal liver and metastases. *Eur Radiol* **23**, 428–434 (2013).
15. Wang, M. *et al.* Evaluation of hepatic tumors using intravoxel incoherent motion diffusion-weighted MRI. *Med. Sci. Monit.* **22**, 702–709 (2016).
16. Colagrande, S. *et al.* Focal liver lesion classification and characterization in noncirrhotic liver: A prospective comparison of diffusion-weighted magnetic resonance-related parameters. *J. Comput. Assist. Tomogr.* **37**, 560–567 (2013).
17. Doblas, S. *et al.* Determination of malignancy and characterization of hepatic tumor type with diffusion-weighted magnetic resonance imaging: Comparison of apparent diffusion coefficient and intravoxel incoherent motion-derived measurements. *Invest. Radiol.* **48**, 722–728 (2013).
18. Ichikawa, S. *et al.* Intravoxel incoherent motion imaging of focal hepatic lesions. *J. Magn. Reson. Imaging* **37**, 1371–1376 (2013).
19. Luo, M., Zhang, L., Jiang, X. & Zhang, W. Intravoxel incoherent motion diffusion-weighted imaging: Evaluation of the differentiation of solid hepatic lesions. *Transl. Oncol.* **10**, 831–838 (2017).
20. Coenegrachts, K. *et al.* Evaluation of true diffusion, perfusion factor, and apparent diffusion coefficient in non-necrotic liver metastases and uncomplicated liver hemangiomas using black-blood echo planar imaging. *Eur. J. Radiol.* **69**, 131–138 (2009).
21. Mürtz, P. *et al.* Accurate IVIM model-based liver lesion characterisation can be achieved with only three b-value DWI. *Eur. Radiol.* **28**, 4418–4428 (2018).
22. Mürtz, P. *et al.* Intravoxel incoherent motion model-based analysis of diffusion-weighted magnetic resonance imaging with 3 b-values for response assessment in locoregional therapy of hepatocellular carcinoma. *OncoTargets Ther.* **9**, 6425–6433 (2016).
23. Mürtz, P. *et al.* Is liver lesion characterisation by simplified IVIM DWI also feasible at 3.0 T?. *Eur. Radiol.* **29**, 5889–5900 (2019).
24. Pieper, C. C. *et al.* Incidence and risk factors of early arterial blood flow stasis during first radioembolization of primary and secondary liver malignancy using resin microspheres: An initial single-center analysis. *Eur. Radiol.* **26**, 2779–2789 (2016).
25. Pieper, C. C. *et al.* Evaluation of a simplified intravoxel incoherent motion (IVIM) analysis of diffusion-weighted imaging for prediction of tumor size changes and imaging response in breast cancer liver metastases undergoing radioembolization: A retrospective single center analysis. *Medicine (Baltimore)* **95**, 1–9 (2016).
26. Pieper, C. *et al.* The value of intravoxel incoherent motion model-based diffusion-weighted imaging for outcome prediction in resin-based radioembolization of breast cancer liver metastases. *OncoTargets Ther.* **9**, 4089–4098 (2016).
27. Pieper, C. C., Sprinkart, A. M., Kukuk, G. M. & Mürtz, P. Short-term measurement repeatability of a simplified intravoxel incoherent motion (IVIM) analysis for routine clinical diffusion-weighted imaging in malignant liver lesions and liver parenchyma at 1.5 T. *RöFo Fortschritte Auf Dem Geb. Röntgenstrahlen Bildgeb. Verfahr.* **191**, 199–208 (2019).
28. Ma, C. *et al.* Effect of region of interest size on ADC measurements in pancreatic adenocarcinoma. *Cancer Imaging* **17**, 13 (2017).
29. Gity, M., Moradi, B., Arami, R., Arabkheradmand, A. & Kazemi, M. A. Two different methods of region-of-interest placement for differentiation of benign and malignant breast lesions by apparent diffusion coefficient value. *Asian Pac. J. Cancer Prev.* **19**, 2765–2770 (2018).
30. Bickel, H. *et al.* Diffusion-weighted imaging of breast lesions: Region-of-interest placement and different ADC parameters influence apparent diffusion coefficient values. *Eur. Radiol.* **27**, 1883–1892 (2017).
31. Suo, S. *et al.* Characterization of breast masses as benign or malignant at 3.0T MRI with whole-lesion histogram analysis of the apparent diffusion coefficient. *J. Magn. Reson. Imaging* **43**, 894–902 (2016).
32. Bruix, J. & Sherman, M. Management of hepatocellular carcinoma: An update. *Hepatology* **53**, 1020–1022 (2011).
33. Robin, X. *et al.* pROC: An open-source package for R and S+ to analyze and compare ROC curves. *BMC Bioinformatics* **12**, 1–8 (2011).
34. DeLong, E. R., DeLong, D. M. & Clarke-Pearson, D. L. Comparing the areas under two or more correlated receiver operating characteristic curves: A nonparametric approach. *Biometrics* **44**, 837–845 (1988).
35. Tamada, T. *et al.* Apparent diffusion coefficient values of prostate cancer: Comparison of 2D and 3D ROIs. *Am. J. Roentgenol.* **210**, 113–117 (2018).
36. Chiaradia, M. *et al.* Intravoxel incoherent motion (IVIM) MR imaging of colorectal liver metastases: Are we only looking at tumor necrosis?. *J Magn Reson Imaging* **39**, 317–325 (2014).
37. Li, H. *et al.* Preoperative histogram analysis of intravoxel incoherent motion (IVIM) for predicting microvascular invasion in patients with single hepatocellular carcinoma. *Eur. J. Radiol.* **105**, 65–71 (2018).
38. Fan, C. *et al.* Discrimination between benign and malignant testicular lesions using volumetric apparent diffusion coefficient histogram analysis. *Eur. J. Radiol.* **126**, 108939 (2020).
39. Donati, O. F. *et al.* Prostate cancer aggressiveness: Assessment with whole-lesion histogram analysis of the apparent diffusion coefficient. *Radiology* **271**, 143–152 (2014).
40. Horvath-Rizea, D. *et al.* The value of whole lesion ADC histogram profiling to differentiate between morphologically indistinguishable ring enhancing lesions-comparison of glioblastomas and brain abscesses. *Oncotarget* **9**, 18148–18159 (2018).
41. Lu, S. S. *et al.* Histogram analysis of apparent diffusion coefficient maps for differentiating primary CNS lymphomas from tumefactive demyelinating lesions. *Am. J. Roentgenol.* **204**, 827–834 (2015).
42. Kang, Y. *et al.* Gliomas: Histogram analysis of apparent diffusion coefficient maps with standard- or high-b-value diffusion-weighted MR imaging—Correlation with tumor grade. *Radiology* **261**, 882–890 (2011).
43. Pathak, R. *et al.* Considering tumour volume for motion corrected DWI of colorectal liver metastases increases sensitivity of ADC to detect treatment-induced changes. *Sci. Rep.* **9**, 3828 (2019).

Author contributions

N.M.: Conception and design of the study, data acquisition, analysis and interpretation, drafted the manuscript. P.M.: Conception and design of the study, data acquisition, analysis and interpretation, drafted the manuscript. A.M.S.: Data analysis and interpretation, critical revision of the manuscript. W.B.: Data analysis and interpretation, critical revision of the manuscript. J.A.L.: Data interpretation, critical revision of the manuscript. U.A.: Data interpretation, critical revision of the manuscript. C.C.P.: Conception and design of the study, data acquisition, analysis and interpretation, critical revision of the manuscript. All authors: Approval of final version of submitted manuscript. P.M. and C.C.P. are guarantors of integrity of the entire study.

Funding

Open Access funding enabled and organized by Projekt DEAL.

Competing interests

The authors declare no competing interests.

Additional information

Supplementary Information The online version contains supplementary material available at https://doi.org/10.1038/s41598-021-01108-6.

Correspondence and requests for materials should be addressed to C.C.P.

Reprints and permissions information is available at www.nature.com/reprints.

Publisher's note Springer Nature remains neutral with regard to jurisdictional claims in published maps and institutional affiliations.

2.2. 2nd publication

Mürtz et al. European Radiology Experimental (2021) 5:33
https://doi.org/10.1186/s41747-021-00233-1

European Radiology Experimental

ORIGINAL ARTICLE Open Access

Simplified intravoxel incoherent motion diffusion-weighted MRI of liver lesions: feasibility of combined two-colour index maps

Petra Mürtz*†, Narine Mesropyan†, Alois M. Sprinkart, Wolfgang Block, Julian A. Luetkens, Ulrike Attenberger and Claus C. Pieper

Abstract

Background: To evaluate the feasibility of two-colour index maps containing combined diffusion and perfusion information from simplified intravoxel incoherent motion (IVIM) for liver lesion malignancy assessment.

Methods: Diffusion-weighted data from a respiratory-gated 1.5-T magnetic resonance sequence were analysed in 109 patients with liver lesions. With three *b* values (0, 50, 800 s/mm^2) estimated diffusion coefficient D′, perfusion fraction f′, and apparent diffusion coefficient (ADC) maps were calculated and analysed for regions of interest (ROIs). D′ and f′ cutoff values were determined by differentiating haemangiomas from other lesions and focal nodular hyperplasias from other lesions, respectively. Combined I_{Df} index maps were generated with a voxel value set to 100, if both D′ and f′ voxel values were lower than their cutoff values (1,529.4 × 10^{-6} mm^2/s and 114.4 × 10^{-3}, respectively), otherwise to 0. Moreover, I_{ADC} index maps were generated from ADC cutoff value (1,338.5 × 10^{-6} mm^2/s) obtained by differentiating benign from malignant lesions. Discriminatory power was assessed for both I_{Df} and I_{ADC}. Index maps were displayed as two-colour overlays to *b*-800 images and visually assessed within the translucent hyperintense areas.

Results: For I_{Df}, the same diagnostic accuracy was achieved as for the combined use of parameters D′ and f′ (93.6%). Compared to I_{ADC}, I_{Df} showed a higher diagnostic accuracy. Visual judgment of I_{Df} yielded an accuracy (95.4%) similar to that of quantitative analysis (93.6%).

Conclusion: Voxel-wise combined two-colour index maps I_{Df} provide similar diagnostic accuracy as ROI-based combination of estimated IVIM parameters D′ and f′ and are suitable for visual assessment of liver lesion malignancy.

Keywords: Diffusion magnetic resonance imaging, Feasibility studies, Focal nodular hyperplasias, Hemangioma, Liver neoplasms

Key points

- Index map I_{Df} can replace the combined use of D and f parameters.
- Two-colour *b*-800 overlay I_{Df} enables a visual assessment of liver lesion malignancy.
- Visual judgment and quantitative analysis of I_{Df} showed comparable diagnostic accuracy.

* Correspondence: petra.muertz@ukb.uni-bonn.de
†Petra Mürtz and Narine Mesropyan contributed equally to this work.
Department of Diagnostic and Interventional Radiology, University Hospital Bonn, Venusberg-Campus 1, D-53127 Bonn, Germany

Background

Diffusion-weighted imaging (DWI) is an important magnetic resonance imaging (MRI) technique for detection

and differentiation of liver lesions not needing contrast agent administration and should be implemented in standard liver examination in routine clinical practice [1].

While DWI acquired with a low *b* value ("black blood" images) provides high sensitivity for lesion detection [2, 3], the apparent diffusion coefficient (ADC) determined from at least two *b* values between 0 and 500–1000 s/mm^2 is usually used for lesion characterisation [4, 5]. The intravoxel incoherent motion (IVIM) concept enables the separation of diffusion and perfusion effects on the DWI signal by assuming a biexponential behaviour of signal intensity [6–8]. The true diffusion coefficient D, the pseudodiffusion coefficient D*, and the perfusion fraction f, reflecting the relative contribution of perfusion to the DWI signal, are often determined by fit algorithms [9]. These require a high number of *b* values and thus relatively long acquisition times. Limited data quality due to signal variations caused by respiratory and cardiac motion and due to low signal-to-noise ratio may lead to unstable fitting results, measurement errors, and poor reproducibility [10–13]. Improved stability and lower acquisition times can be achieved by so-called "simplified IVIM", which uses explicit computation of IVIM numerically stable parameter estimations in combination with a small number of *b* values. Simplified IVIM turned out to be valuable for liver lesion characterisation and assessment of therapy in clinical routine [3, 14–20].

For lesion assessment, voxel-wise evaluation and the creation of parameter maps are important. Still somewhat inconvenient for clinical use is the quantitative analysis of regions of interests (ROI) in the IVIM parameter maps. The use of colour-coded maps [21, 22] as overlay over b_0 DWI images [14–16, 23] enables visual lesion assessment. For the assessment of malignancy, knowledge of the cutoff values of each IVIM parameter is necessary. From ischemic stroke diagnostic using computed tomography perfusion, the use of two-colour index maps is known allowing a rapid and easy image interpretation [24, 25]. Suitable two-colour index maps obtained from IVIM parameters could allow a rapid and easy image interpretation with respect to malignancy.

The purpose of this study was to create and evaluate two-colour index maps, which combines diffusion and perfusion information obtained by simplified IVIM for convenient visual assessment of liver lesion malignancy.

Methods

Study cohort

This retrospective study was approved by the local institutional review board of the University Hospital Bonn, Germany, with waiver for written informed patient consent. Data of 1,721 consecutive examinations (from February 2013 to September 2016) of patients, who received a 4 *b* value DWI sequence at 1.5 T, were reviewed. Data of 1350 examinations were not used because the patients had no liver lesions, only cysts, or lesions < 1 cm, or because it was not the first examination in the study time frame, so that data of 371 different patients with at least one focal liver lesion ≥ 1 cm other than cysts were included. Of these 371 patients, 262 (70.6%) were excluded due to lack of a definitive diagnosis based on histology or typical imaging characteristics (n = 46), local treatment of the liver (n = 143), insufficient image quality caused by motion artifacts (n = 27) or pixel misalignments (n = 5), unfavourable lesion location as close to prior biopsy or drainage tracts or at the edge of the liver (n = 6), partial volume of an adjacent slice (n = 10), or difficulties to identify the lesions on DWI (n = 5). In the presence of a combination of (non-cystic) benign lesions and malignant disease, patients were excluded because malignant disease may affect the appearance of benign liver lesions, *e.g.*, due to thrombosis (n = 20). Finally, data of 109 patients were analysed (Table 1).

These patients had already been examined in an upcoming study by Mesropyan et al and in a previous study [15], where basic investigations concerning simplified IVIM for liver lesion characterisation [15] and different ROI placement and analysis methods had been performed in an upcoming study by Mesropyan et al. In the present study, the data were used to evaluate two-colour index maps constructed with the help of IVIM parameter analysis results.

Cholangiocellular carcinomas (CCCs) were histologically proven. Hepatocellular carcinomas (HCCs) were either histologically proven or diagnosed according to the American Association for the Study for Liver Disease MRI criteria [26]. Diagnosis of metastasis was histologically proven or based on typical imaging features in combination with histologically proven primary cancer. Diagnosis of focal nodular hyperplasia (FNH) or haemangioma was established based on typical radiological findings on contrast-enhanced MRI and was confirmed by at least one follow-up examination.

Magnetic resonance imaging

Imaging was performed on a clinical whole-body 1.5-T MRI system (Ingenia, Philips Healthcare, Eindhoven, The Netherlands) equipped with powerful gradient system (45 mT/m maximum amplitude, 200 T/m/s maximum slew rate) and 32-channel abdominal coil with digital interface for signal reception. DWI with a respiratory-triggered single-shot spin-echo echo-planar imaging variant (Table 2) with four *b* values (0, 50, 250, 800 s/mm^2) was applied before contrast agent administration. Isotropic diffusion-weighted images were reconstructed by from the images with diffusion-sensitised gradients in three orthogonal directions on the MRI system.

Table. 1 Group composition and demographic data of included subjects

Liver pathologies	Total number of patients	Number of males	Age range (years)
Hepatocellular carcinoma	32	20	55–87
Cholangiocellular carcinoma	8	4	57–85
Metastases from colorectal cancer	22	17	47–87
Metastases from breast cancer	12	0	48–70
Haemangioma	23	12	34–84
Focal nodular hyperplasia	12	1	14–54
Total	109	54	14–87

Postprocessing

IVIM parameters D and f as well as conventional ADC were calculated voxel-wise from b = 0, 50, and 800 s/mm^2 by using the following approximations:

$$D' = ADC(50,800) = \frac{\ln(S(b_{50})) - \ln(S(b_{800}))}{b_{800} - b_{50}} \quad (1)$$

$$f' = f(0,50,800) = 1 - \frac{S(b_{50})}{S(b_0)} \cdot exp^{D' \cdot b_{50}} \quad (2)$$

$$ADC = ADC(0,800) = \frac{\ln(S(b_0)) - \ln(S(b_{800}))}{b_{800} - b_0} \quad (3)$$

Parameter maps and two-colour index maps (see below) were calculated offline using custom written software in MATLAB (MathWorks, Natick, Massachusetts, USA).

Image analysis

Image analysis by ROIs was performed by a radiologist (N.M.) with 3 years of experience and checked by a radiologist (C.C.P.) with 10 years of experience in abdominal imaging and a physicist (P.M.) with more than 20 years of experience in DWI. All were blinded to clinical information. One reference lesion per lesion type was analysed. A two-dimensional ROI was placed centrally in each lesion on a single representative slice. This slice was largely unaffected by motion and susceptibility artifacts and pixel misalignments and not at the rim of the lesion to avoid partial volume effects. ROIs were drawn as large as possible using DWI with the highest contrast between lesion and normal tissue. Central necrosis, cystic components, and scars as found by hyperintensities on b0 images and/or hypointensities on b-800 images were excluded in an upcoming study by Mesropyan et al. After visually cross-checking for pixel misalignments between images with different b values, the ROI was analysed in the related parameter maps ADC, D′, and f′ and saved for later use (see below).

Construction of two-colour index maps

Two-colour index maps I_{ADC}, I_D, and I_f were constructed from suitable cutoff values for ADC, D′, and f′, respectively. The cutoff values were determined as previously introduced [14, 15]: the ADC cutoff value was determined by receiver operating characteristic (ROC)

Table. 2 Technical parameters of the diffusion-weighted imaging (DWI) sequence

Name	Value
Field of view (right-left × anterior-posterior)/orientation	380 × 326 mm/transversal
Slice number/thickness/gap	30/7.0 mm/0.7 mm
Matrix/resolution	112 × 94/3.4 × 3.5 mm
Echo time	63 ms
Repetition time	1 respiratory cycle
Imaging time per respiration	1,600 ms
Echo-planar imaging/half-Fourier/SENSE factor	51/0.6/2
Diffusion gradients	3 orthogonal directions
b values (number of averages per direction)	0, 50, and 250 s/mm^2 (2); 800 s/mm^2 (4)
Fat suppression methods	Spectral presaturation by inversion recovery, SPIR
Water-fat shift/bandwidth	9.2 pixel/23.6 Hz
Bandwidth in echo-planar imaging frequency direction	1,437.9 Hz
Acquisition time	Around 4 min (2:42 min:s without gating)

SENSE Parallel imaging with sensitivity encoding

analysis of malignant and benign lesion groups; for the combined use of D′ and f′, the D' cutoff value was determined by differentiation between haemangiomas and all other lesions and the f′ cutoff value by differentiation between FNHs and all other lesions. Motivated by the high diffusion coefficient of haemangiomas [14, 15, 27, 28] and the high perfusion fraction of FNHs [14, 15, 29], lesions were assigned as malignant if ROI-wise mean values of D′ and f′ were both below their cutoff values, and otherwise as benign. In the index maps, a voxel value was set to 100 if the corresponding parameter voxel value was lower than the determined cutoff value; otherwise, the voxel value was set to 0. By combining I_D and I_f, the index map I_{Df} was generated. For I_{Df}, a voxel value was set to 100 if the corresponding voxel values of I_D and I_f were both 100; otherwise, the voxel value was set to 0. Voxel values 0 and 100 were displayed in green and red, respectively, indicating benign and malignant structures. These index maps were displayed as overlay over the DWI *b*-800 images.

Evaluation of the two-colour index maps

First, to ensure that the voxel-wise consideration of the cutoff values does not worsen diagnostic performance compared to ROI-wise, for I_{ADC}, I_D, and I_f, the same ROC analysis was performed as for the related original parameter (see the "Construction of two-colour index maps" section). AUC values were compared pairwise. Second, to compare the diagnostic performance of ADC, D′, and f′ as well as of I_{Df}, I_{ADC}, and ADC, all maps were quantitatively analysed using ROIs (see the "Image analysis" section). ROC analyses of the benign and malignant lesion groups were then performed. AUC values were compared with each other.

Third, the I_{ADC} and I_{Df} index maps were evaluated visually by one investigator (P.M.). The visual assessment was restricted to areas of translucent hyperintensity from DWI *b*-800 images, whereby necrosis, cystic components, and scars identified as hyperintense areas on *b*-0 images and/or hypointense areas on *b*-800 images were excluded. A four-point scale was used, as follows: (1) definitely malignant, if the red voxels dominated definitely; (2) probably malignant, if red voxels dominated only slightly; (3) probably benign, if green voxels dominated only slightly; and (4) definitely benign, if green voxels dominated definitely.

The accuracy of I_{ADC} and I_{Df} for lesion differentiation by visual assessment was determined and compared with each other and with ADC.

The assessment was repeated after 4 months by the same investigator (P.M.) and by a second independent investigator (C.C.P.).

Statistical analysis

Statistically significant differences ($p < 0.05$) between groups (independent samples) were tested in SPSS (version 24.0, IBM, Armonk, New York , USA) by using Student *t* test or non-parametric Mann–Whitney *U* test, depending on whether the data were normally distributed or not. In order to differentiate between two groups, ROC analysis was performed using pROC package in R (version 1.17.0.1, open source package, accessible at http://expasy.org/tools/pROC/ under the GNU General Public License) [30]. Youden's index was used to determine the optimal cutoff value of the ROC curve providing the highest combination of sensitivity and specificity. DeLong method was used to compare the area under the curve (AUC) of dependent and independent ROC curves [31]. The intraclass correlation coefficients (ICCs) were calculated for the visual assessment results of the same investigators (ICC_{intra}) and of the two different investigators (ICC_{inter}).

Results

Examples of DWI and two-colour index maps are given in Figs. 1 and 2.

Verification of voxel-wise cutoff value applicability

ROC analysis of ROI-based analysed index maps and related original parameter maps revealed similar AUC values (Table 3). The comparison of AUC values revealed no significant differences, as expected, neither between I_{ADC} and ADC in discriminating benign from malignant lesions (0.958 *versus* 0.945, $p = 0.196$), nor between I_D and D′ in discriminating haemangiomas from all other lesions (0.985 *versus* 0.985, $p = 1.000$), nor between I_f and f′ in discriminating FNHs and all other lesions (0.968 *versus* 0.974, $p = 0.294$).

Quantitative evaluation of index maps I_{ADC} and I_{Df}

All parameter values were significantly lower for malignant lesions than for benign (Table 4), *e.g.*, for ADC 1, 124 ± 180 × 10^{-6} mm^2/s (mean ± standard deviation) *versus* 1,692 ± 313 × 10^{-6} mm^2/s ($p < 0.001$). Accordingly, for all index values, the numbers of red voxels were significantly higher for malignant than for benign lesions, *e.g.*, for I_{ADC} 80% ± 21% *versus* 17% ± 25% ($p < 0.001$) and for I_{Df} 76% ± 17% *versus* 20% ± 18% ($p < 0.001$).

As can be seen in Table 4, among the single parameters ADC, D', and f′, the ADC was best suited to discriminate benign and malignant lesions. The AUC value of ADC was significantly higher than that of D′ (0.958 *versus* 0.902, $p = 0.001$) and f′ (0.958 *versus* 0.622, $p < 0.001$), AUC of D′ was significantly higher than that of f′ (0.902 *versus* 0.622, $p = 0.001$). By ADC, 89.9% of the lesions were correctly identified as malignant and benign

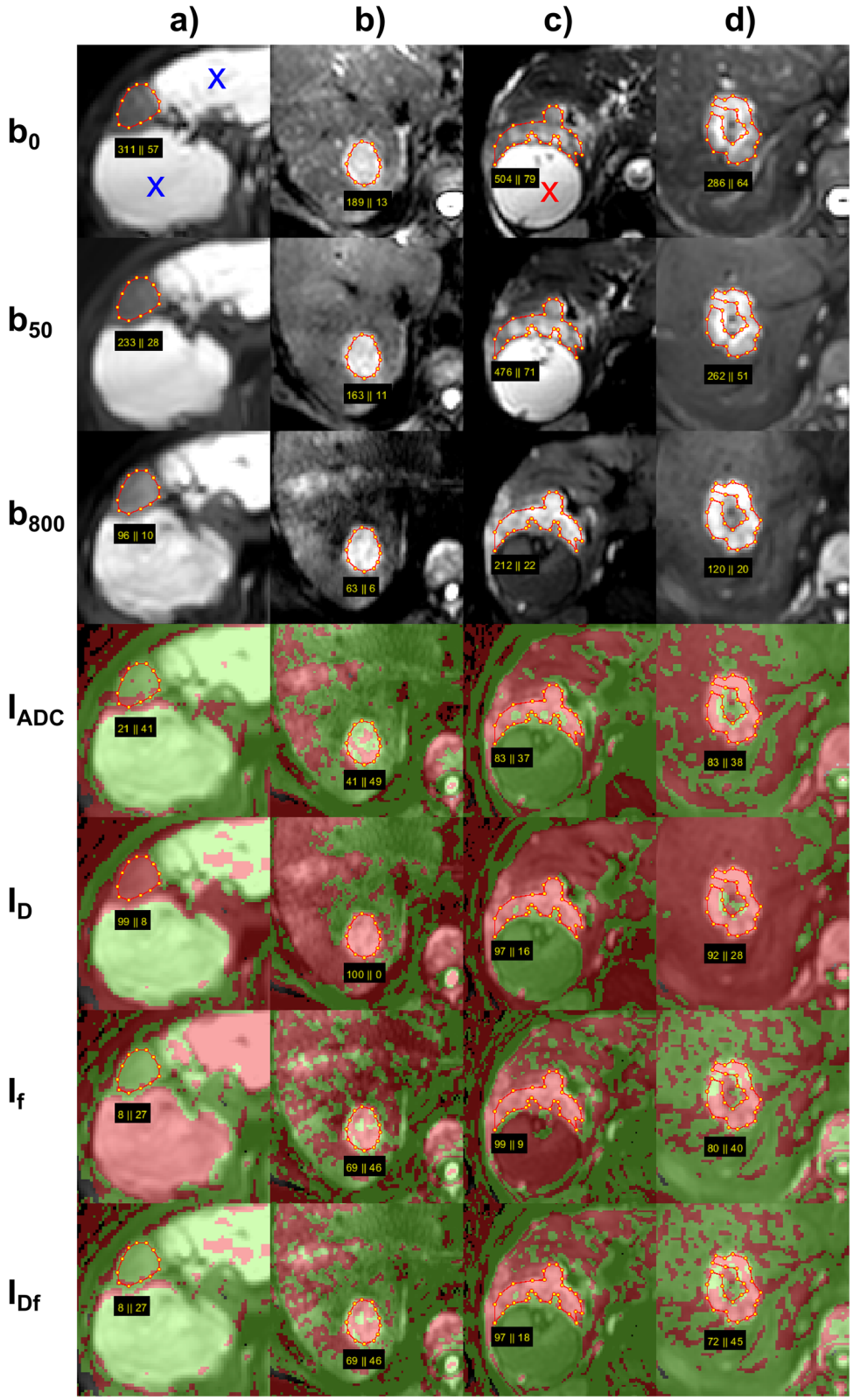

Fig. 1 (See legend on next page.)

(See figure on previous page.)
Fig. 1 Typical examples of two-colour index maps. Combined index maps I_{Df} are given in comparison to index maps I_{ADC} together with I_D and I_f, overlaid to *b*-800 images, for (**a**) FNH together with two haemangiomas (blue x), (**b**) HCC, (**c**) CCC together with bilioma (red x), and (**d**) metastasis from colorectal carcinoma (CRC). The FNH reveals almost everywhere voxels with perfusion fraction above cutoff (I_f green) so that I_{Df} shows clear benignity despite diffusion coefficient below cutoff (I_D red), I_{ADC} showed slightly less green voxels compared to I_{Df} (79% *versus* 92%). The haemangiomas shows almost everywhere voxels with diffusion coefficient above cutoff (I_D green), so that I_{Df} shows clear benignity despite the low perfusion fraction (I_f red), the same is valid for I_{ADC}. The HCC shows area-wide diffusion coefficient below cutoff (red I_D), and mainly perfusion fraction below cutoff with heterogeneous distribution (I_f scattered red) and thus also I_{Df} showing clear malignancy, I_{ADC} shows less red voxels compared to I_{Df} (41% *versus* 69%) showing benignity, the visual assessment was "probably" benign. The CCC appears on all maps mainly red showing clear malignancy on I_{Df} and I_{ADC} maps. The bilioma looks identical to the haemangiomas. The CRC reveals mainly red voxels within the selected region of interest, which excluded hypointense region on *b*-800 image (necrosis). *CCC* Cholangiocellular carcinoma, *CRC* Metastasis from colorectal carcinoma, *FNH* Focal nodular hyperplasia, *HCC* Hepatocellular carcinoma

(cutoff value 1,338.5 × 10^{-6} mm^2/s). By using the combination of D′ and f′, 93.6% of the lesions were correctly identified (cutoff values 1,529.4 × 10^{-6} mm^2/s and 114.4 × 10^{-3}, respectively), which was an improvement compared to ADC.

Comparing the AUC values of I_{Df} and I_{ADC}, larger values were found for I_{Df} than for I_{ADC} (0.975 *versus* 0.945), but differences were not significant (p = 0.168). The diagnostic accuracy was higher for I_{Df} than for I_{ADC}. With I_{Df} 93.6% of the lesions (cutoff value 50.2%) were correctly identified as benign and malignant, with I_{ADC} 88.1% (cutoff value 53.4%). Falsely identified cases by I_{Df} *versus* I_{ADC} were 1 *versus* 2 FNHs, 1 *versus* 1 haemangiomas, 4 *versus* 3 HCCs, 0 *versus* 1 CCCs, and 1 *versus* 6 metastases. I_{Df} was superior to I_{ADC} especially in case of metastases identifying 5 cases correctly as malignant, which were falsely assigned as benign by I_{ADC}.

Visual evaluation of index maps I_{ADC} and I_{Df}

By visual judgment of I_{Df} and I_{ADC} maps within translucent hyperintensity from DWI *b*-800 images (Table 5), a similar number of lesions were correctly identified as by quantitative analysis using ROIs excluding central necrosis, cystic components, and scars (95.4% instead of 93.6% for I_{Df} and 90.8% instead of 88.1% for I_{ADC}). As in the quantitative analysis, the reached diagnostic accuracy was higher for I_{Df} than for I_{ADC}. With I_{Df} 95.4% of the lesions were correctly identified, with I_{ADC} 90.8%. The assignment was "definite" in 87.2% for I_{Df} and in 89.9% for I_{ADC} and "probable" in 12.8% for I_{Df} and in 10.1% for I_{ADC}. "Probable" assignment by I_{Df} and I_{ADC} was mainly found for FNHs (4 and 7, respectively) and HCCs (4 and 6, respectively) and only rarely for haemangiomas (0 and 1, respectively), CCCs (1 and 0, respectively), and metastases (2 and 0, respectively). Falsely identified cases by I_{Df} *versus* I_{ADC} were 2 *versus* 5 FNHs, 1 *versus* 1 haemangiomas, 1 *versus* 3 HCCs, 0 *versus* 0 CCCs, and 1 *versus* 1 metastasis. I_{Df} was superior to I_{ADC} especially in case of FNHs and HCCs identifying 3 FNHs and 2 HCCs correctly, which were falsely assigned by I_{ADC}. Examples are given in Fig. 1b, Fig. 2a, and Fig. 2b. Visual judgment of I_{Df} was superior especially in case of HCCs identifying 4 HCCs correctly, which were falsely assigned by quantitative analysis. Visual judgment of I_{ADC} was superior especially in case of metastases but inferior in case of FNHs identifying 5 metastases correctly, which were falsely assigned by quantitative analysis, and 3 FNHs falsely (as "probable malignant"), which were correctly identified by quantitative analysis.

The repeated analysis by the same investigator and by the independent investigator (see Table 5) revealed excellent intraobserver and interobserver reliability (ICC_{intra} 0.992 for I_{ADC} and 0.989 for I_{Df}; ICC_{inter} 0.986 for I_{ADC} and 0.977 for I_{Df}).

Discussion

In this study, simplified IVIM was used to create combined two-colour index maps I_{Df} from parameters D′ and f′ as overlay to *b*-800 images in order to facilitate visual assessment of liver lesions. Red voxels show diffusion and perfusion restrictions and indicate malignancy in combination with translucent *b*-800 hyperintensity. The main result was that the voxel-wise combination of D′ and f′ thresholds in the form of the I_{Df} index map provides identical diagnostic accuracy as the ROI-based combined analysis of the D′ and f′ parameter maps. A higher diagnostic accuracy was found for I_{Df} than for I_{ADC} (created from ADC). Visual judgment of the I_{Df} index map as two-colour overlay to *b*-800 images showed comparable diagnostic accuracy than quantitative analysis of I_{Df}.

In previous simplified IVIM studies on liver lesions at 1.5 and 3.0 T it was found that ADC is the best single parameter to discriminate between malignant and benign liver lesions but that improved discriminatory power could be reached by combined use of D′ and f′ [14, 15]. This result was confirmed in the present study. Compared to the previous 1.5-T study [15], which was performed on the same patient group than the present study but with new ROI analysis, higher diagnostic accuracy was reached, for ADC (89.9% *versus* 82.1%) and for combined D′ and f′ (93.6% *versus* 85.6%). In the present study, one reference ROI per lesion type and patient was included, in the previous study up to 5 lesions

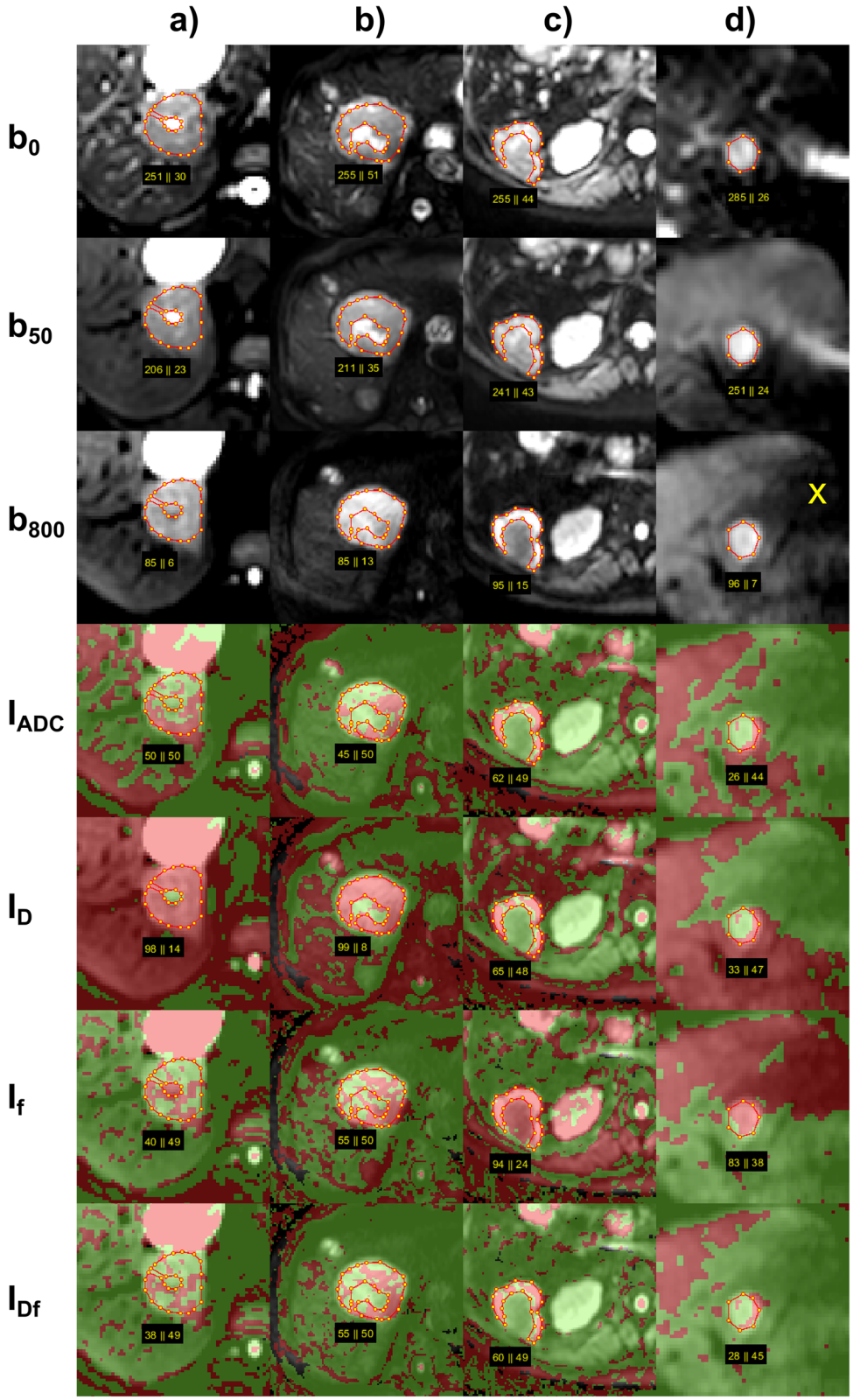

Fig. 2 (See legend on next page.)

(See figure on previous page.)
Fig. 2 Further examples of combined two-colour index maps. Combined index maps I_{Df} are given in comparison to index maps I_{ADC} together with I_D and I_f, overlaid to *b*-800 images, for (**a**) FNH, (**b**) HCC, (**c**) metastasis of breast cancer, and (**d**) HCC. The FNH with central scar (**a**) and the HCC with central necrosis (**b**) show similar behaviour on all index maps with nearly all voxels being red on I_D and about half of the voxels being red with scattered distribution on I_f and also on I_{ADC} and I_{Df}. On I_{ADC}, visual assessment of FNH is "probable malignant" and of HCC "probably benign," which is wrong in both cases. Quantitative values are both (50% and 45%, respectively) just below the threshold to malignancy (at 53%) leading to correct assignment for FNH and wrong for HCC. On I_{Df}, visual assessment of FNH is "probable benign" and of HCC "probably malignant," which is correct in both cases. Quantitative values (38% and 55%, respectively) were below and above threshold (50%), respectively, leading also to correct assignments. The metastasis with central necrosis (**c**) shows only a small margin of vital tumour, which can be easier captured by visible judgment than by ROI analysis with unclear tissue boundary. The HCC (**d**) shows the typical behaviour of a haemangioma (see Fig. 1a) and the assignment is false negative. However, the hypointense area of the left liver lobe adjacent to the lesion on *b*-800 indicates motion influences, which raise the diffusion coefficient of the liver tissue and lesion artificially as can be seen on I_D, I_{ADC}, and I_{Df} index maps. *CCC* Cholangiocellular carcinoma, *FNH* Focal nodular hyperplasia, *HCC* Hepatocellular carcinoma

per lesion type and patient were included and averaged for analysis (clustered analysis). Necrotic areas, liquids, and scares were excluded from ROIs in both studies, but can also be excluded retrospectively by automatically selecting voxels with low diffusion coefficients with the help of histogram analysis of D′ (upcoming study by Mesropyan et al).

New in the present work is the creation and evaluation of the index maps I_{Df}, which combine the information from D′ and f′, use only two colours, and are presented as overlay to *b*-800 in order to be able to assess only the vital tumour areas by translucent hyperintensity and to exclude necrosis, cystic components, and scars from assessment. Up to now, colour-coded maps with more than two colours have been used for the different IVIM parameters [13, 21, 22, 32], sometimes presented as overlays to b0 images [14, 15]. Whether the ROI-wise obtained and combined cutoff values of D′ and f′ would also work voxel-wise in I_{Df} was not clear in advance. Perfusion and diffusion restrictions do not necessarily have to occur in the same voxels. But the fact that I_{Df} provided identical diagnostic accuracy than combined use of D′ and f′ (93.6% *versus* 93.6%) means that the ROI-wise obtained cutoff values of the parameters can be applied voxel-wise in the index maps.

For I_{Df} higher accuracy was reached than for I_{ADC}, by quantitative analysis (93.6% *versus* 88.1%) and by visual judgment (95.4% *versus* 90.8%). The relative good performance of I_{ADC} is due to the fact that for liver lesion differentiation diffusion and perfusion influences act in the same direction.

When visually assessing two-colour index maps, it is only necessary to distinguish whether more or less than half of the voxels in the tumour areas of interest are red. This allows a rapid and easy image interpretation also for less skilled operators. Excellent intraobserver and interobserver reliability was achieved. By visual judgment comparable diagnostic accuracy was reached than by ROI-based quantitative analysis, for I_{Df} (95.4% *versus* 93.6%) and I_{ADC} (90.8% *versus* 88.1%). The assignment malignant/benign was "definite" in about 90% of the cases and "probable" in about 10%, for I_{Df} and I_{ADC}. Some of the FNHs showed relatively high numbers of red voxels on I_{Df} with scattered distribution caused by heterogeneous perfusion as can be seen on I_f index map. Those FNHs looked similar to typical HCCs (Fig. 2a, b).

Table. 3 Receiver operating characteristic analysis for construction of index maps

Parameter	Mean ± SD	Mean ± SD	*p* value	Dir	AUC	95% Confidence interval	Cutoff	Sen	Spec	Acc
	Malignant (*n* = 74)	Benign (*n* =35)								
ADC	1,124 ± 180	1,692 ± 313	< 0.001	>	0.958	0.922–0.993	1,338.5	0.892	0.914	0.899
I_{ADC}	80 ± 21	17 ± 25	< 0.001	<	0.945	0.894–0.996	53.4	0.865	0.914	0.881
	All other (*n* = 86)	HAEMs (*n* = 23)								
D′	1,076 ± 184	1,784 ± 314	< 0.001	>	0.985	0.965–1.000	1,529.4	0.988	0.913	0.972
I_D	95 ± 12	20 ± 25	< 0.001	<	0.985	0.966–1.000	51.0	0.988	0.913	0.972
	All other (*n* = 97)	FNHs (*n* = 12)								
f′	63 ± 35	164 ± 58	< 0.001	>	0.968	0.938–0.998	114.5	0.907	1.000	0.917
I_f	82 ± 17	32 ± 17	< 0.001	<	0.974	0.947–1.000	54.6	0.918	1.000	0.927

Mean values and standard deviations of apparent diffusion coefficient (ADC), estimated diffusion coefficient (D′), estimated perfusion fraction (f′), and index maps I_{ADC}, I_D, and I_f are presented. The optimal cutoff point of ROC analysis was selected according to maximum Youden index. ADC and D′ values are given in units of 10^{-6} mm^2/s, f′ values are given in units of 10^{-3}, and I_{ADC}, I_D, and I_f are given as percentages. *Acc* Accuracy, *ADC* Apparent diffusion coefficient, *AUC* Area under the curve, *Dir* Test direction (">"/"<" means that a lower/higher test result indicates a more positive test), *FNH* Focal nodular hyperplasias, *HAEM* Haemangioma, *SD* Standard deviation, *Sens* Sensitivity, *Spec* Specificity

Table. 4 Receiver operating characteristic analysis for differentiation of malignant from benign liver lesions

Parameter	Malignant (n = 74) Mean ± SD	Benign (n = 35) Mean ± SD	p value	Dir	AUC	95% Confidence interval	Cutoff	Sen	Spec	Acc
ADC	1,124 ± 180	1,692 ± 313	< 0.001	>	0.958	0.922–0.993	1,338.5	0.892	0.914	0.899
D′	1,057 ± 188	1,580 ± 387	< 0.001	>	0.902	0.842–0.962	1,173.6	0.757	0.886	0.798
f′	63 ± 31	97 ± 70	0.010	>	0.622	0.491–0.754	114.5	0.932	0.457	0.780
I_{ADC}	80 ± 21	17 ± 25	< 0.001	<	0.945	0.894–0.996	53.4	0.865	0.914	0.881
I_D	94 ± 12	47 ± 43	< 0.001	<	0.782	0.672–0.891	51.0	0.986	0.600	0.862
I_f	81 ± 16	65 ± 30	0.032	<	0.627	0.499–0.756	57.0	0.905	0.457	0.761
I_{Df}	76 ± 17	20 ± 18	< 0.001	<	0.975	0.950–1.000	50.2	0.932	0.943	0.936

Mean values and standard deviations of apparent diffusion coefficient (ADC), estimated diffusion coefficient (D′), estimated perfusion fraction (f′), and index maps I_{ADC}, I_D, I_f and combined I_{Df} are presented. The optimal cutoff point of ROC analysis was selected according to maximum Youden index. ADC and D′ values are given in units of 10^{-6} mm^2/s, f′ values are given in units of 10^{-3}, and I_{ADC}, I_D, I_f, and I_{Df} are given as percentages. *Acc* Accuracy, *ADC* Apparent diffusion coefficient, *AUC* Area under the curve, *Dir* Test direction (">"/"<" means that a lower/higher test result indicates a more positive test), *SD* Standard deviation, *Sens* Sensitivity, *Spec* Specificity

Visual assessment of those lesions was less accurate than ROI-based quantitative analysis. Metastases, on the other hand, often have only a narrow margin of vital tumour tissue, so that an exact ROI positioning is difficult leading to less accurate results in case of quantitative analysis compared to visual assessment (Fig. 2c).

General concerns regarding the simplified IVIM approach as for example the b value choice have already been addressed in the previous studies [14, 15]. Only three of the four acquired b values were used, because no diagnostic added value was found for the fourth *b* value (250 s/mm^2) and the determination of D* [14, 15]. Simplified IVIM parameter calculations by using approximations and explicit formulas instead of fitting procedures are simple and stable and lead to reliable information. Exceptions are as generally low signal-to-noise ratios (*e.g.*, patients with hemochromatosis or fatty liver), small lesions (partial volume effects), or presence of artifacts. Due to motion influences artificially enlarged D′ and reduced f′ values may be measured, especially for the left liver lobe and on slices close to the heart. It is important to check the surrounding liver in the *b*-800 image for signal loss (Fig. 2d). Since the IVIM parameter f depends on the relaxation times, f may vary with field strength and sequence parameters used (especially b values, echo times, and repetition times) [33, 34], this also applies to the cutoff points used for the index maps. The new combined two-colour index maps I_{Df} were checked on the same patients who provided the cutoff points for generation in order to enable a direct comparison with the combined use of the parameter maps D′ and f′. A validation study is planned on a larger patient cohort, which also includes rarer and atypical lesions as well as lesions difficult to identify in DWI. It is interesting to compare the use of the two-colour index maps I_{Df} with full set of conventional protocol in terms of reading time and reader confidence.

Table. 5 Results of visual judgment of index maps I_{ADC}, I_D, I_f, and combined I_{Df}

Parameter	Definite				Probable				All					
	TN	FN	FP	TP	TN	FN	FP	TP	N	P	T	Sen	Spec	Acc
Investigator 1														
I_{ADC}	28	2	3	65	1	2	3	5	35	74	109	0.946	0.829	0.908
I_D	22	1	13	73	0	0	0	0	35	74	109	0.986	0.629	0.872
I_f	6	1	23	73	4	0	2	0	35	74	109	0.986	0.286	0.761
I_{Df}	26	2	1	66	6	0	2	6	35	74	109	0.973	0.914	0.954
Investigator 1 repeated after 4 months														
I_{ADC}	28	2	3	65	1	2	3	5	35	74	109	0.946	0.829	0.908
I_{Df}	26	2	1	66	6	0	2	6	35	74	109	0.973	0.914	0.954
Investigator 2														
I_{ADC}	28	2	3	65	1	2	3	5	35	74	109	0.946	0.829	0.908
I_{Df}	26	2	1	66	6	0	2	6	35	74	109	0.973	0.914	0.954

Acc Accuracy, *FN* False negative cases, *FP* False positive cases, *N* Number of benign cases (TN + FP), *P* Number of malignant cases (TN + FP), *T* Total number of cases (N + P), *TN* True negative cases, *Sen* Sensitivity, *Spec* Specificity, *TP* True positive cases

In conclusion, the voxel-wise combined index maps I_{Df} and the ROI-based combination of D′ and f′ parameters provide concordant diagnostic accuracy for the differentiation of malignant and benign liver lesions. The I_{Df} index map used as two-colour overlay to *b*-800 images can be considered as a new tool for visual assessment of liver lesion malignancy.

Abbreviations

ADC: Apparent diffusion coefficient; AUC: Area under the curve; CCC: Cholangiocellular carcinoma; CRC: Metastasis from colorectal carcinoma; D′: Estimated diffusion coefficient; DWI: Diffusion-weighted imaging; f′: Estimated perfusion fraction; FNH: Focal nodular hyperplasia; HCC: Hepatocellular carcinoma; I_{ADC}: ADC index maps; ICC: Intraclass correlation coefficient; I_D: D′ index maps; I_{Df}: D′ and f′ combined index maps; I_f: f′ index maps; IVIM: Intravoxel incoherent motion; MRI: Magnetic resonance imaging; ROC: Receiver operating characteristic; ROI: Region of interest

Authors' contributions

Study concept: PM and CP; manuscript preparation and editing: PM, CP, NM, AS, and UA; data acquisition and analysis: NM, PM, CP, AS, WB, and JL. The authors read and approved the final manuscript.

Funding

The authors state that this work has not received any funding. Open Access funding enabled and organised by Projekt DEAL.

Availability of data and materials

The datasets used and/or analysed during the current study are available from the corresponding author on reasonable request.

Declarations

Ethics approval and consent to participate

The local institutional review board of the University Hospital Bonn, Germany, approved the retrospectively performed IVIM analysis of DWI MRI data from clinical routine examinations (reference number 303/16).

Consent for publication

Not applicable.

Competing interests

The authors declare that they have no competing interests.

Received: 3 May 2021 Accepted: 3 July 2021
Published online: 09 August 2021

References

1. Taouli B (2012) Diffusion-weighted MR imaging for liver lesion characterization: a critical look. Radiology 262:378–380. https://doi.org/10.1148/radiol.11112417
2. Takahara T, Kwee TC (2012) Low b-value diffusion-weighted imaging: emerging applications in the body. J Magn Reson Imaging 35:1266–1273. https://doi.org/10.1002/jmri.22857
3. Coenegrachts K, Delanote J, Ter Beek L et al (2009) Evaluation of true diffusion, perfusion factor, and apparent diffusion coefficient in non-necrotic liver metastases and uncomplicated liver hemangiomas using black-blood echo planar imaging. Eur J Radiol 69:131–138. https://doi.org/10.1016/j.ejrad.2007.09.013
4. Miller FH, Hammond N, Siddiqi AJ, et al (2010) Utility of diffusion-weighted MRI in distinguishing benign and malignant hepatic lesions. J Magn Reson Imaging 32:138–147. https://doi.org/10.1002/jmri.22235
5. Parikh T, Drew SJ, Lee VS, et al (2008) Focal liver lesion detection and characterization with diffusion-weighted MR imaging: comparison with standard breath-hold T2-weighted imaging. Radiology 246:812–822. https://doi.org/10.1148/radiol.2463070432
6. Padhani AR, Liu G, Koh DM et al (2009) Diffusion-weighted magnetic resonance imaging as a cancer biomarker: consensus and recommendations. Neoplasia 11:102–125. https://doi.org/10.1593/neo.81328
7. Koh DM, Collins DJ, Orton MR (2011) Intravoxel incoherent motion in body diffusion-weighted MRI: reality and challenges. AJR Am J Roentgenol 196:1351–1361. https://doi.org/10.2214/AJR.10.5515
8. Guiu B, Cercueil JP (2011) Liver diffusion-weighted MR imaging: the tower of Babel? Eur Radiol 21:463–467. https://doi.org/10.1007/s00330-010-2017-y
9. Le Bihan D, Breton E, Lallemand D et al (1988) Separation of diffusion and perfusion in intravoxel incoherent motion MR imaging. Radiology 168:497–505. https://doi.org/10.1148/radiology.168.2.3393671
10. Andreou A, Koh DM, Collins DJ, et al (2013) Measurement reproducibility of perfusion fraction and pseudodiffusion coefficient derived by intravoxel incoherent motion diffusion-weighted MR imaging in normal liver and metastases. Eur Radiol 23:428–434. https://doi.org/10.1007/s00330-012-2604-1
11. Kakite S, Dyvorne H, Besa C, et al (2015) Hepatocellular carcinoma: short-term reproducibility of apparent diffusion coefficient and intravoxel incoherent motion parameters at 3.0T. J Magn Reson Imaging 41:149–156. https://doi.org/10.1002/jmri.24538
12. Cho GY, Kim S, Jensen JH, Storey P, Sodickson DK, Sigmund EE (2012) A versatile flow phantom for intravoxel incoherent motion MRI. Magn Reson 67:1710–1720. https://doi.org/10.1002/mrm.23193
13. Lee Y, Lee SS, Kim N, et al (2015) Intravoxel incoherent motion diffusion-weighted MR imaging of the liver: effect of triggering methods on regional variability and measurement repeatability of quantitative parameters. Radiology 274:405–415. https://doi.org/10.1148/radiol.14140759
14. Mürtz P, Pieper CC, Reick M, et al (2019) Is liver lesion characterisation by simplified IVIM DWI also feasible at 3.0 T? Eur Radiol 29:5889–5900. https://doi.org/10.1007/s00330-019-06192-x
15. Mürtz P, Sprinkart AM, Reick M, et al (2018) Accurate IVIM model-based liver lesion characterisation can be achieved with only three b-value DWI. Eur Radiol 28:4418–4428. https://doi.org/10.1007/s00330-018-5401-7
16. Penner A-H, Sprinkart AM, Kukuk GM, et al (2013) Intravoxel incoherent motion model-based liver lesion characterisation from three b-value diffusion-weighted MRI. Eur Radiol 23:2773–2783. https://doi.org/10.1007/s00330-013-2869-z
17. Pieper C, Meyer C, Sprinkart AM, et al (2016) The value of intravoxel incoherent motion model-based diffusion-weighted imaging for outcome prediction in resin-based radioembolization of breast cancer liver metastases. Onco Targets Ther 9:4089–4098. https://doi.org/10.2147/OTT.S104770
18. Mürtz P, Penner A-H, Pfeiffer A-K, et al (2016) Intravoxel incoherent motion model-based analysis of diffusion-weighted magnetic resonance imaging with 3 b-values for response assessment in locoregional therapy of hepatocellular carcinoma. Onco Targets Ther 9:6425–6433. https://doi.org/10.2147/OTT.S113909
19. Pieper CC, Sprinkart AM, Meyer C, et al (2016) Evaluation of a simplified intravoxel incoherent motion (IVIM) analysis of diffusion-weighted imaging for prediction of tumor size changes and imaging response in breast cancer liver metastases undergoing radioembolization: a retrospective single center analysis. Medicine (Baltimore) 95:e3275. https://doi.org/10.1097/MD.0000000000003275
20. Pieper CC, Willinek WA, Meyer C, et al (2016) Intravoxel incoherent motion diffusion-weighted MR imaging for prediction of early arterial blood flow stasis in radioembolization of breast cancer liver metastases. J Vasc Interv Radiol 27:1320–1328. https://doi.org/10.1016/j.jvir.2016.04.018
21. Wang M, Li X, Zou J, Chen X, Chen S, Xiang W (2016) Evaluation of hepatic tumors using intravoxel incoherent motion diffusion-weighted MRI. Med Sci Monit 22:702–709. https://doi.org/10.12659/MSM.895909
22. Luo M, Zhang L, Jiang X, Zhang W (2017) Intravoxel incoherent motion diffusion-weighted imaging: evaluation of the differentiation of solid hepatic lesions. Transl Oncol 10:831–838. https://doi.org/10.1016/j.tranon.2017.08.003
23. Concia M, Sprinkart AM, Penner A-H, et al (2014) Diffusion-weighted magnetic resonance imaging of the pancreas: diagnostic benefit from an intravoxel incoherent motion model-based 3 b-value analysis. Invest Radiol 49:93–100. https://doi.org/10.1097/RLI.0b013e3182a71cc3
24. Ukmar M, Degrassi F, Pozzi Mucelli RA, Neri F, Mucelli FP, Cova MA (2017) Perfusion CT in acute stroke: effectiveness of automatically-generated colour maps. Br J Radiol 90:1–10. https://doi.org/10.1259/bjr.20150472

25. Lin L, Bivard A, Parsons MW (2013) Perfusion patterns of ischemic stroke on computed tomography perfusion. J Stroke 15:164–173. https://doi.org/10.5853/jos.2013.15.3.164
26. Bruix J, Sherman M, Llovet JM, et al (2001) Clinical management of hepatocellular carcinoma. Conclusions of the Barcelona-2000 EASL conference. European Association for the Study of the Liver. J Hepatol 35:421–430. https://doi.org/10.1016/s0168-8278(01)00130-1
27. Choi IY, Lee SS, Sung YS, et al (2017) Intravoxel incoherent motion diffusion-weighted imaging for characterizing focal hepatic lesions: correlation with lesion enhancement. J Magn Reson Imaging 45:1589–1598. https://doi.org/10.1002/jmri.25492
28. Zhu L, Cheng Q, Luo W, Bao L, Guo G (2015) A comparative study of apparent diffusion coefficient and intravoxel incoherent motion-derived parameters for the characterization of common solid hepatic tumors. Acta Radiol 56:1411–1418. https://doi.org/10.1177/0284185114559426
29. Luo M, Zhang L, Jiang X-H, Zhang W-D (2017) Intravoxel incoherent motion: application in differentiation of hepatocellular carcinoma and focal nodular hyperplasia. Diagn Interv Radiol 23:263–271. https://doi.org/10.5152/dir.2017.16595
30. Robin X, Turck N, Hainard A, et al (2011) pROC: an open-source package for R and S+ to analyze and compare ROC curves. BMC Bioinformatics 12:1–8. https://doi.org/10.1186/1471-2105-12-77
31. DeLong ER, DeLong DM, Clarke-Pearson DL (1988) Comparing the areas under two or more correlated receiver operating characteristic curves: a nonparametric approach. Biometrics 44:837–845. https://doi.org/10.2307/2531595
32. Ter Voert EEGW, Delso G, Porto M et al (2016) Intravoxel incoherent motion protocol evaluation and data quality in normal and malignant liver tissue and comparison to the literature. Invest Radiol 51:90–99. https://doi.org/10.1097/RLI.0000000000000207
33. Grech-Sollars M, Hales PW, Miyazaki K, et al (2015) Multi-centre reproducibility of diffusion MRI parameters for clinical sequences in the brain. NMR Biomed 28:468–485. https://doi.org/10.1002/nbm.3269
34. Lemke A, Laun FB, Simon D, Stieltjes B, Schad LR (2010) An in vivo verification of the intravoxel incoherent motion effect in diffusion-weighted imaging of the abdomen. Magn Reson Med 64:1580–1585. https://doi.org/10.1002/mrm.22565

Publisher's Note

3. Acknowledgments

I would like to thank Dr. Claus C. Pieper and PhD Petra Mürtz for their excellent leadership during the data acquisition, analysis, interpretation as well as manuscripts` preparation. Also, I would like to thank Prof. Ulrike I. Attenberger and Dr. Julian A. Luetkens for their support in realizing the entire project.

4. List of publications

1. **Mesropyan N**, Kupczyk P, Dold L, Praktiknjo M, Chang J, Isaak A, Endler C, Kravchenko D, Bischoff LM, Sprinkart AM, Pieper CC, Kuetting D, Attenberger U, Luetkens JA**.** Assessment of liver cirrhosis severity with extracellular volume fraction MRI. Sci Rep 2022 doi:10.1038/s41598-022-13340-9
2. **Mesropyan N**, Isaak A, Dabir D, Hart C, Faron A, Endler C, Kravchenko D, Katemann C, Pieper CC, Kuetting D, Attenberger U, Luetkens JA. Free-breathing high resolution modified Dixon steady-state angiography with compressed sensing for the assessment of the thoracic vasculature in pediatric patients. JCMR 202
3. **Mesropyan N*,** Mürtz P*, Sprinkart AM, Block W, Luetkens JA, Attenberger U, Pieper CC. Simplified intravoxel incoherent motion (IVIM) for liver lesion characterization – Comparison of different ROI analysis methods. Sci Rep 2021
4. Mürtz P*, **Mesropyan N*,** Sprinkart AM, Block W, Luetkens JA, Attenberger U, Pieper CC. Simplified intravoxel incoherent motion diffusion-weighted MRI of liver lesions: feasibility of combined two-colour index maps. Eur Radiol Exp 2021: 5(1). doi:10.1186/s41747-021-00233-1.
5. **Mesropyan N**, Kupczyk P, Isaak A, Endler C, Dold L, Sprinkart AM, Pieper CC, Kuetting D, Attenberger U, Luetkens JA**.** Synthetic extracellular volume fraction without hematocrit sampling for hepatic applications. Abdom Radiol 2021: 46(10):4637–46. doi:10.1007/s00261-021-03140-6.
6. **Mesropyan N**, Kupczyk P, Kukuk GM, Dold L, Weismueller T, Endler C, Isaak A, Faron A, Sprinkart AM, Pieper CC, Kuetting D, Strassburg CP, Attenberger U, Luetkens JA. Diagnostic value of magnetic resonance parametric mapping for non-invasive assessment of liver fibrosis in patients with primary sclerosing cholangitis. BMC Med Imaging 2021: 21(1). doi:10.1186/s12880-021-00598-0.
7. **Mesropyan N**, Kupczyk P, Dold L, Weismüller TJ, Sprinkart AM, Mädler B, et al. Non-invasive assessment of liver fibrosis in autoimmune hepatitis: Diagnostic value of liver magnetic resonance parametric mapping including extracellular volume fraction. Abdom Radiol 2021:46(6):2458–66. doi:10.1007/s00261-020-02822-x.
8. Nowak S*, **Mesropyan N***, Faron A, Block W, Reuter M, Attenberger U, Luetkens JA, Sprinkart AM. Detection of liver cirrhosis in standard T2-weighted MRI using deep

transfer learning. Eur Radiol. 2021 DOI:10.1007/s00330-021-07858-1. doi:10.1007/s00330-021-07858-1.

9. **Mesropyan N**, Isaak A, Faron A, Praktiknjo M, Jansen C, Kuetting D, Meyer C, Pieper CC, Sprinkart AM, Chang J, Maedler B, Thomas D, Kupczyk P, Attenberger U, Luetkens JA. Magnetic resonance parametric mapping of the spleen for non-invasive assessment of portal hypertension. Eur Radiol 2020: 31(1):85–93. doi:10.1007/s00330-020-07080-5.
10. Luetkens JA, Voigt M, Faron A, Isaak A, **Mesropyan N**, Dabir D, Sprinkart AM, Pieper CC, Chang J, Attenberger U, Kuetting D, Thomas D. Influence of hydration status on cardiovascular magnetic resonance myocardial T1 and T2 relaxation time assessment: an intraindividual study in healthy subjects. J Cardiovasc Magn Reson. 2020 Sep 7;22(1):63. doi: 10.1186/s12968-020-00661-9.
11. Luetkens JA, Isaak A, Öztürk C, **Mesropyan N**, Monin M, Schlabe S, Reinert M, Faron A, Heine A, Velten M, Dabir D, Boesecke C, Strassburg CP, Attenberger U, Zimmer S, Duerr GD, Nattermann J. Cardiac MRI in Suspected Acute COVID-19 Myocarditis. Radiol Cardiothorac Imaging. 2021 Mar 4;3(2):e200628. eCollection 2021 Apr doi: 10.1148/ryct.2021200628.
12. Faron A, Isaak A, **Mesropyan N**, Reinert M, Schwab K, Sirokay J, Sprinkart AM, Bauernfeind FG, Dabir D, Pieper CC, Heine A, Kuetting D, Attenberger U, Landsberg J, Luetkens JA. Cardiac MRI Depicts Immune Checkpoint Inhibitor-induced Myocarditis: A Prospective Study Radiology. 2021 Sep 28; 210814 doi: 10.1148/radiol.2021210814
13. Isaak A, Bischoff LM, Faron A, Endler C, **Mesropyan N**, Sprinkart AM, Pieper CC, Kuetting D, Dabir D, Attenberger U, Luetkens JA. Multiparametric cardiac magnetic resonance imaging in pediatric and adolescent patients with acute myocarditis. Pediatr Radiol. 2021 Aug 25. doi: 10.1007/s00247-021-05169-7.
14. Kravchenko D, Isaak A, Zimmer S, **Mesropyan N**, Reinert M, Faron A, Pieper CC, Heine A, Velten M, Nattermann J, Kuetting D, Duerr GD, Attenberger UI, Luetkens JA. Cardiac MRI in Patients with Prolonged Cardiorespiratory Symptoms after Mild to Moderate COVID-19 Infection. Radiology. 2021 Aug 10:211162. doi: 10.1148/radiol.2021211162.

15. Isaak A, Luetkens JA, Faron A, Endler C, **Mesropyan N**, Katemann C, Zhang S, Kupczyk P, Kuetting D, Attenberger U, Dabir D. J Free-breathing non-contrast flow-independent cardiovascular magnetic resonance angiography using cardiac gated, magnetization-prepared 3D Dixon method: assessment of thoracic vasculature in congenital heart disease. Cardiovasc Magn Reson. 2021 Jul 19;23(1):91. doi: 10.1186/s12968-021-00788-3.
16. Endler CH, Ginzburg D, Isaak A, Faron A, **Mesropyan N**, Kuetting D, Pieper CC, Kupczyk PA, Attenberger UI, Luetkens JA. Diagnostic Benefit of MRI for Exclusion of Ligamentous Injury in Patients with Lateral Atlantodental Interval Asymmetry at Initial Trauma CT. Radiology. 2021 Sep;300(3):633-640. doi: 10.1148/radiol.2021204187.
17. Endler CH, Faron A, Isaak A, Katemann C, **Mesropyan N**, Kupczyk PA, Pieper CC, Kuetting D, Hadizadeh DR, Attenberger UI, Luetkens JA. Fast 3D Isotropic Proton Density-Weighted Fat-Saturated MRI of the Knee at 1.5 T with Compressed Sensing: Comparison with Conventional Multiplanar 2D Sequences. Rofo. 2021 Jul;193(7):813-821. doi: 10.1055/a-1337-3351.

* Shared first autorship